University of Zurich[UZH]

Bachelor Thesis

A Search for Neutron Disappearance in GERDA Experiment

Author:
Aline Schneuwly

Supervised by:
Prof. Dr. Laura Baudis
Dr. Junting Huang

August 31, 2021

Acknowledgements

I would like to thank all those who have supported me in the realisation of this thesis.
Firstly, I would like to thank Prof. Dr. Laura Baudis for giving me the opportunity to work on this interesting project and to dive into the exciting field of particle astrophysics. Further, I gratefully thank my supervisor, Dr. Junting Huang, for his patient guidance, his encouragement throughout the course of this work and for introducing me to ROOT, Geant4 and the use of remote clusters. Thanks to you, I have learned a lot during this project. Finally, I would like to thank my family and friends for their support.

Contents

1 Introduction

Baryon number is seemingly accidentally conserved in the Standard Model (SM). A violation of this quantum number is strongly motivated from many distinct theoretical considerations, including the idea of unification of particles and forces [1] and the observed baryon asymmetry of the universe [2]. According to J. Heeck and V. Takhistov, nuclear decays are envisioned to be the best probe for baryon number-violating searches [2]. Such experimental searches have been conducted for more than two decades [3] and they are of fundamental importance to learn about physics beyond the SM.
A total of 75 possible nucleon decay modes respecting the conservation laws of electric charge, energy-momentum and angular momentum are identified by the Particle Data Group [4]. While most of the lifetime limits for these modes lie above 10^{30} years, there are a few significant exceptions with lifetime limits of several orders of magnitude lower. These modes correspond to the decay of one or two neutrons into neutrinos: $n \to 3\nu$, $n \to 5\nu$ and $nn \to 2\nu$ [4]. The importance of the single neutron disappearance for the exploration of baryon number-violation is underlined by the study of J. Heeck and V. Takhistov [2].

There is an additional interest to this problem. It could be that the neutron disappearance is related to the neutron lifetime puzzle. This is a 4σ discrepancy between the lifetime measured with the neutrons stored in a bottle and the lifetime measured with a neutron beam. A theory proposes that this difference in lifetime may be caused by neutrons decaying into particles that are not detected in the beam experiments, i.e. invisible particles. Proton-based measurements can then give a longer lifetime [5].

The significance of this project is that a search on the single neutron decay channel with germanium nuclei has never been conducted before in this field.

The aim of this thesis is to set a limit on the lifetime of single neutron disappearance in ^{76}Ge. The first chapter introduces the physics behind the phenomenon of neutron disappearance. In the next chapter, the GERDA neutrinoless double beta decay experiment is described. Based on a Geant4 simulation, the signal efficiency is calculated in chapter three. In a next step, a subset of GERDA data is analysed in chapter four, in order to select candidate events. In chapter five, a statistical analysis is conducted to set the lower limit on the lifetime of neutron disappearance. The last chapter closes the thesis with a conclusion and an outlook on future improvements to the analysis.

2 Physics Background

2.1 Matter-Antimatter Asymmetry

Over 13.7 billion years ago when our universe was born, matter and antimatter were created in equal amount. As the universe expands, temperature decreases and the universe moves away from equilibrium. Matter and antimatter annihilate into radiation. The reverse of this process is prohibited since the radiation energy drops below the pair production threshold. The fact that not everything in the universe is just radiations necessitates an excess of matter over antimatter in the annihilation process [6]. Finding the origin of this matter-antimatter asymmetry has been, and still is, the driving force for a large number of research programs in physics [7].

2.2 Baryon Number Violation

In 1967, A. Sakharov first introduced three necessary conditions (Sakharov conditions) to explain the observed matter-antimatter asymmetry of the universe. Besides C and CP violation and departure from thermal equilibrium, the violation of baryon number is one of these conditions. This violation is one of the key prerequisites for successful baryogenesis, the physical process that has hypothetically produced the observed baryon-antibaryon asymmetry or the imbalance between matter (baryons) and antimatter (antibaryons) in the universe [8].
Another motivation to search for baryon number violating processes stems from various grand unification theories (GUTs) [9]. These theories unify the three forces of the Standard Model into a single gauge group. Associated baryon number violation are the defining predictions of the GUTs [2].

There are many potential nucleon decay channels in which the baryon number is violated. The Particle Data Group identifies 75 possible decay modes that respect the conservation laws of electric charge, momentum and energy [4]. A selection of possible decay channels is presented in Figure 1.
Despite more than two decades of experimental investigation, no processes violating baryon number have been observed yet. However, there are many reasons to believe that this symmetry could be broken [2].

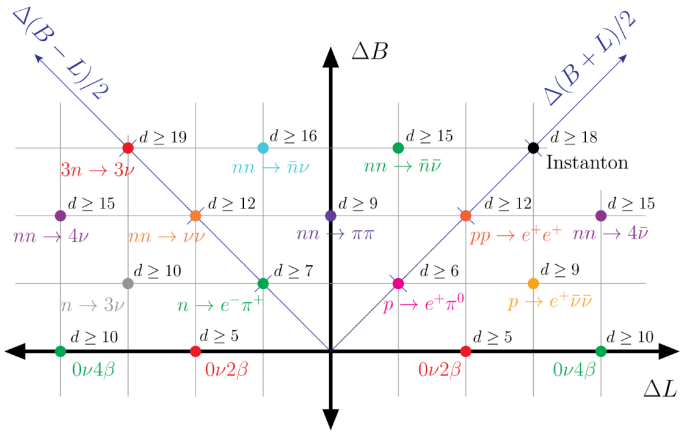

Figure 1: Processes with baryon and lepton number violation by units of ΔB and ΔL, respectively. The figure is taken from [2].

2.3 Invisible Neutron Decay

Baryon instability can lead to a disappearance of a neutron from its intra-nucleus state into any undetectable particles [3]. Examples of such particles are neutrinos or dark matter particles. This process is referred to as invisible neutron decay or neutron disappearance [3]. A possible dark decay channel is illustrated in Figure 2, where χ is a dark matter particle, $\Phi = (3,1)_{-1/3}$ is a scalar and ϕ is a complex scalar in an attempt to explain the neutron lifetime puzzle in [5].

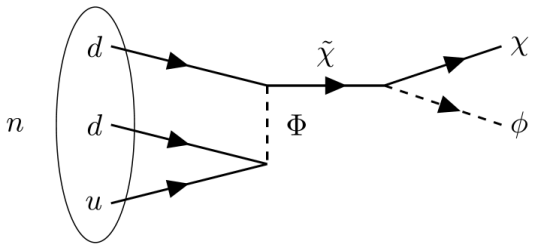

Figure 2: A possible dark decay scenario of the neutron. The figure is taken from [10].

Various experiments have been conducted on ^{16}O and ^{12}C in order to search for neutron disappearance. The following provides an overview of these experiments and their results on the lifetime limits. Table 1 summarizes the existing lifetime limits on single neutron disappearance.

SNO
SNO (Sudbury Neutrino Observatory) was constructed to study the fundamental properties of solar neutrinos. It is located underground at SNOLAB in Sudbury, Canada. The SNO detector target consists of 1 kton of heavy water contained in an acrylic vessel and viewed by over 9'000 photomultiplier tubes. Data taking started in May 1999 and ended in November 2006 [11].
SNO constrained the lifetime for nucleon decay via "invisible" modes, such as $n \to 3\nu$. The source was ^{16}O in heavy-water (D_2O). The disappearance of either a proton or a neutron from the source lead to an excited residual nucleus. Searching for γ-rays from the de-excitation of the residual nucleus was the basis for this analysis. A limit of $\tau_{inv} > 1.9 \times 10^{29}$ year was obtained at 90% C.L. for both invisible neutron and invisible proton decay modes [12].

KamLAND
KamLAND (Kamioka Liquid scintillator Anti-Neutrino Detector) was constructed to investigate neutrino oscillation parameters by observing electron antineutrinos emitted from distant nuclear reactors. KamLAND was located underground at the Kamioka Observatory in Hida, Japan. The detector consisted of 1 kton of highly purified liquid scintillator contained in a transparent nylon-based balloon suspended in non-scintillating mineral oil. Over 1800 photomultiplier tubes were mounted on the inner surface of a stainless steel sphere that enclosed the detector. The experiment started operation in March 2002 and entered the KamLAND-Zen phase for neutrinoless double beta decay ($0\nu\beta\beta$) search in 2011 [13].
The KamLAND experiment searched for invisible decays of neutrons, such as $n \to 3\nu$ or $nn \to 2\nu$. The source was ^{12}C in liquid scintillator. The analysis was based on the observation of a sequence of space and time correlated events resulting from the de-excitation of the corresponding daughter nucleus. Limits of $\tau_{n\to invisible} > 5.8 \times 10^{29}$ year and $\tau_{nn\to invisible} > 1.4 \times 10^{30}$ year at 90% C.L. were obtained [14].

SNO+
The SNO+ experiment is a follow up of the SNO experiment aiming to look for $0\nu\beta\beta$ decay. The construction started in February 2017, reusing the acrylic vessel, the photomultiplier tubes and the electronics of the SNO detector. The acrylic vessel, containing the target medium, is suspended in ultra-pure water. There are three operating phases of the SNO+ experiment, distinguished by the target medium. The water phase with ultra-pure water as a target medium enabled SNO+ to be operated as a Cherenkov detector from May 2017 to July 2019. The ultra-pure water is currently being replaced with liquid scintillator developed by the SNO+ collaboration, marking the beginning of the scintillator phase. The third phase of the experiment will use tellurium-loaded liquid scintillator as the target medium. The SNO+ collaboration also pursues a rich physics program beyond the search for $0\nu\beta\beta$ decay, such as studies of geo- and reactor antineutrinos, supernova and solar neutrinos and the search for invsible nucleon decay [15].

This experiment conducted a search for nucleon decay through invisible modes. The source was ^{16}O in water. The analysis was based on a search for γ-rays emitted at the de-excitation of the daughter that was produced through invisible nucleon decays within the oxygen nucleus. Among other limits for the single neutron decay, a limit of $\tau > 2.5 \times 10^{29}$ year at 90% C.L. was obtained [16].

2.4 Single Neutron Disappearance Search in GERDA

Up to this day, baryon number violation searches on ^{76}Ge nuclei have only been conducted for tri-nucleon decays in the MAJORANA experiment [17]. The single neutron disappearance channel in ^{76}Ge, however, remains unexplored. Thus, in this thesis, this specific decay channel in germanium nuclei in GERDA is explored.

The previous best 90% C.L lifetime lower limits, considered by the Particle Data Group listings of 2020 [4], for bound neutrons decaying into invisibles, are summarized in Table 1.

Decay	Nucleus	Experiment	Year	Limit (year)
$n \rightarrow invisible$	^{16}O	SNO	2004	$> 1.9 \times 10^{29}$
$n \rightarrow invisible$	^{12}C	KamLAND	2006	$> 5.8 \times 10^{29}$
$n \rightarrow invisible$	^{16}O	SNO+	2018	$> 2.5 \times 10^{29}$

Table 1: Existing lifetime limits at 90% C.L. on the single neutron disappearance from various experiments. Data is taken from [4].

3 The GERDA Experiment

The GERDA (GERmanium Detector Array) experiment searches for ($0\nu\beta\beta$) decay of ^{76}Ge nucleus by operating high-purity germanium (HPGe) diodes, isotopically enriched in ^{76}Ge to about 87%, in liquid argon. The germanium serves both as decay source and detector. The experiment provides the world's best lower limit on the half-life of $0\nu\beta\beta$ decay in ^{76}Ge, which is set at $T_{1/2} > 1.8 \times 10^{26}$ yr at 90% C.L. [18].
Data taking started in 2011 with Phase I. After a substantial upgrade campaign, Phase II began in December 2015. There was a minor upgrade in 2018 where new detectors were introduced. Data taking finished in November 2019 with a total exposure of 127.2 kg year [18].
The following section details the experimental setup of GERDA.

3.1 Experimental Setup

The GERDA experiment is operated underground at the Laboratori Nazionali del Gran Sasso (LNGS), one of the largest underground laboratories in the world devoted to neutrino and astroparticle physics, located in central Italy [19]. The rock overburden of 1400 m (equivalent to 3500 m water) reduces the cosmic muon flux by six orders of magnitude to $(3.41 \pm 0.01) \times 10^{-4}\,\mathrm{m}^{-2}\,\mathrm{s}^{-1}$ [20].
The construction and design of GERDA target background minimization. Multiple layers of materials passively and actively shield the germanium detectors. The HPGe detectors are arranged in vertical columns forming an array supported by low-activity silicon holders, shown in Figure 4 and Figure 5. This construct is directly immersed in high-purity liquid argon (LAr), the key design feature of GERDA. The LAr is contained in a $63\,\mathrm{m}^3$ cryostat and acts as a coolant and as background shielding. Additionally, LAr is a very effective scintillator. The LAr volume surrounding the detector array is equipped with photo-detectors and operated as an active LAr veto. To enhance the light collection efficiency, wavelength-shifting fibers are employed. The cryostat is surrounded by a 10 m diameter water tank ($590\,\mathrm{m}^3$ ultra-pure water), which shields external γ and neutron radiation. In order to veto the cosmic muons, the water tank is instrumented with photomultipliers (PMTs) transforming the water volume into a Cherenkov detector. An additional muon veto is provided by plastic scintillator panels installed on the top of the structure. [21, 22]. The experimental setup for GERDA is shown in Figure 3.

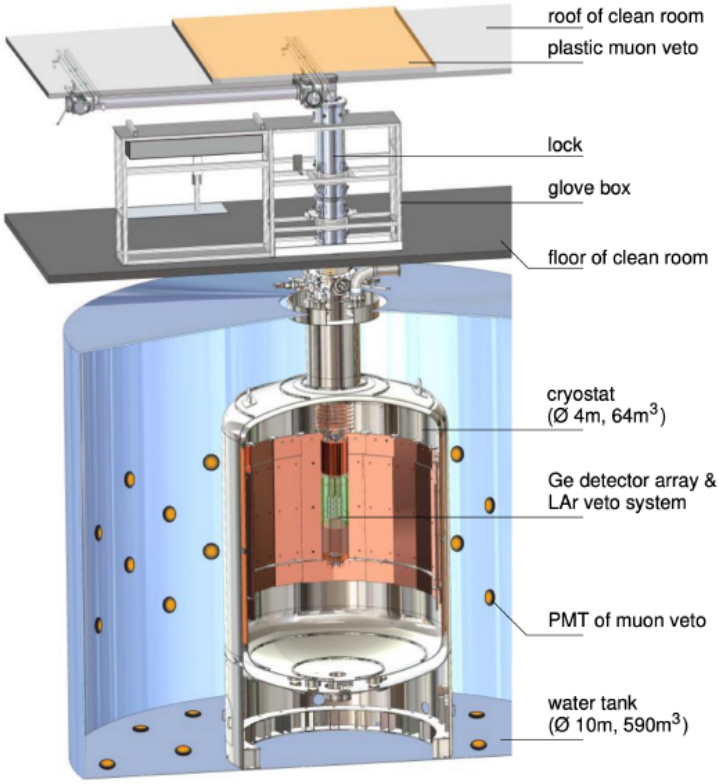

Figure 3: Setup of the GERDA experiment. The figure is taken from [23]

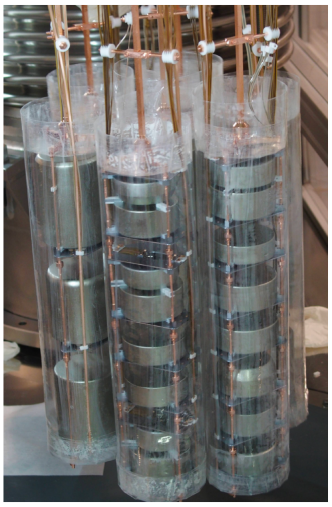

Figure 4: Full assembled Phase II array with nylon mini-shrouds. The figure is taken from [24].

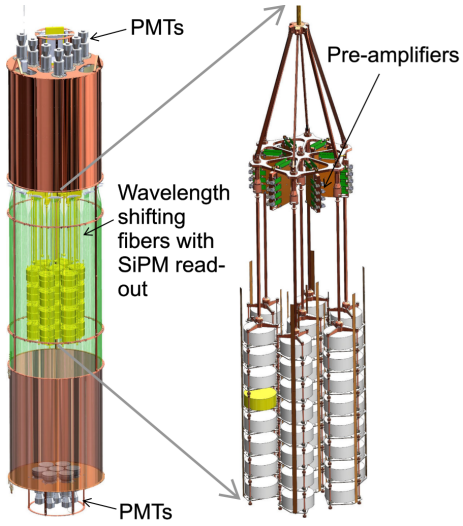

Figure 5: Liquid argon veto instrumentation on the left, germanium detector array with low activity electronics on the right. The figure is taken from [20].

3.2 The GERDA Detectors

In the period between the start of Phase II in December 2015 and the upgrade in 2018, two types of detectors were operated in GERDA: 10 coaxial and 30 Broad Energy Germanium (BEGe). This analysis is based on the data from this period and the above mentioned types of detectors are of importance to this thesis. During the upgrade in 2018, a third type of detector was installed: Inverted Coaxial Point Contact (IC). Five new detectors of this type replaced all three coaxial detectors that have a natural abundance of ^{76}Ge. Photos of these detectors are shown in Figure 6, and schematics of the cross-section are illustrated in Figure 7. The spatial arrangement of the coaxial and BEGe detectors in GERDA Phase II before the 2018 upgrade is shown in Figure 8.

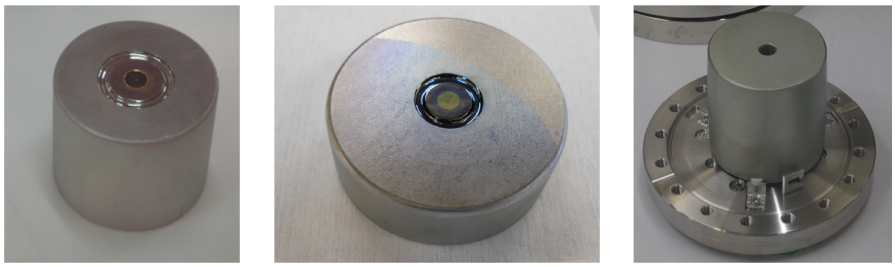

Figure 6: Photos of a coaxial (left), BEGe (centre) and IC (right) detector. The photos are taken from [20].

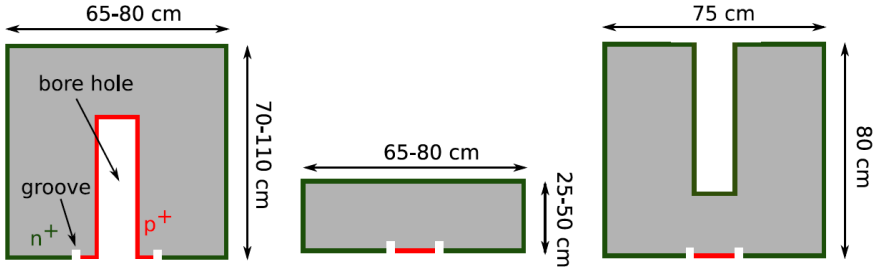

Figure 7: Schematic cross-section of coaxial (left), BEGe (centre) and IC(right) detectors. The electrons and holes created due to particles interaction drift to n+ (green) and p+ (red) electrodes, respectively. The "+" indicates extra concentrations of the dopant. The figure is taken from [20].

The detectors are all read out via their grounded p contact, that is formed by the implantation of boron atoms via an ion beam. The depletion high voltage is applied to the n contact, which is formed by the thermal diffusion of lithium atoms. This region, also known as the dead-layer, shields the detector from surface contaminants such as α particles [20].
The larger coaxial detectors were inherited from HEIDELBERG-MOSCOW and IGEX, experiments which were the previous generation ^{76}Ge $0\nu\beta\beta$ experiments. Their internal borehole forms a large p contact. The total enriched mass of this type of detectors is 15.6 kg [20].
The smaller BEGe detectors were specifically developed for GERDA [25]. Contrary to the coaxial detectors, they do not consist of a borehole but have a $\mathcal{O}(1)$ cm^2 area as their p contact instead. Thus, the electric field is concentrated close to the p contact. As a result, most of the signal is caused by the holes moving in this region. Due to their small electronic capacitance and therefore larger signal-to-noise ratio, the BEGe detectors have a better energy resolution compared to the coaxial detectors. The total enriched mass of the BEGe detectors

is 20.0 kg [20, 25].

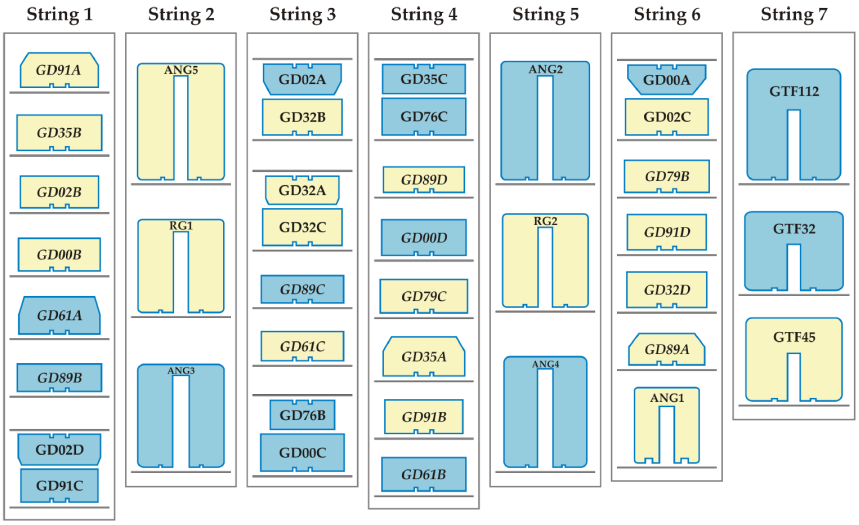

Figure 8: Final detector configuration of the GERDA Phase II germanium detector array before the 2018 upgrade. Detectors in blue are passivated to reduce the current flowing between n+ and p+ electrodes. String 7 is installed in the middle, surrounded by strings 1 to 6 as shown in Figure 10. The figure is taken from [24].

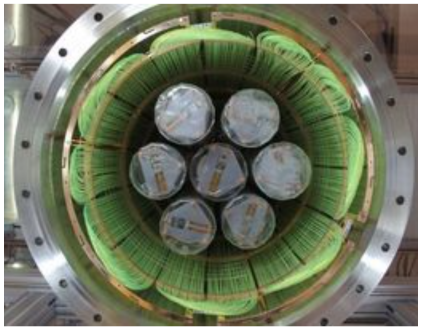

Figure 9: Bottom view of array positioned in fibre shroud. The figure is taken from [24].

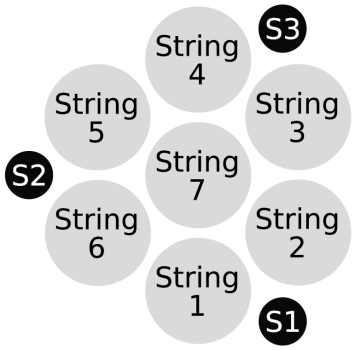

Figure 10: Top view of the detector strings (grey) and calibration sources (black). The figure is taken from [20]

3.3 Neutron Disappearance Search

When a bound neutron inside a ^{76}Ge nucleus decays into particles that are invisible to GERDA detectors, such as dark matter particles or neutrinos, it produces a ^{75}Ge nucleus. The latter then becomes ^{75}As through β^- decay with a half-life time of $T_{1/2} = 83\,\text{min}$. In the de-excitation process of ^{75}As (if it is not already in the ground state) a gamma is emitted [7]. The β decays of ^{75}Ge and the energy levels of ^{75}As are shown in Figure 11.

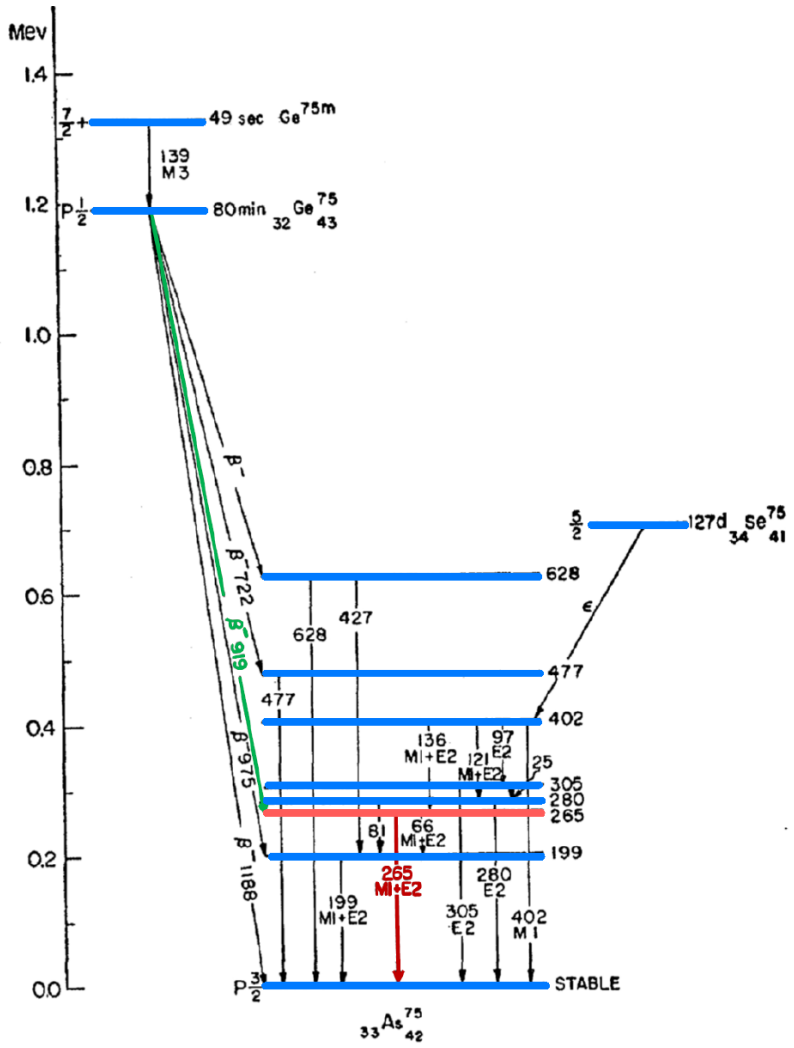

Figure 11: Level scheme of ^{75}As. The level and transition energies are given in keV. The figure is adapted from [26].

Possible signatures of the neutron disappearance from ^{76}Ge in GERDA are the β decay of ^{75}Ge with a Q value of 919 keV (green decay in Figure 11) followed by a 265 keV gamma (red in Figure 11). The branching ratio of this 265 keV gamma is 11.4% [26], much larger than that of other channels with an emitted gamma from an excited state of ^{75}As. By tagging the double coincidence of the β decay in one detector and the 265 keV gamma in its neighbouring detectors, one can select signal events with a very low background expectation. The analysis is presented in detail in the following chapters.

4 Simulation

The aim of this chapter is to calculate the signal efficiency ϵ of the event selection based on a Geant4 simulation.

4.1 MaGe Software

The simulation program used is called MaGe. It is a Geant4-based Monte Carlo simulation software framework for low-background germanium experiments, specifically the GERDA and MAJORANA experiments. The MaGe framework contains, besides the actual experiments, the geometry models of common objects, prototypes and test stands. Additional features that are implemented are Geant4 physics lists, output formats and customized event generators. Advantages of combining all the common classes into one framework are the reduced duplication of efforts, the easier comparison between simulated data and experiment and the simplified addition of new detectors to the simulation [27]. The GERDA setup in Geant4 is shown in Figure 12.

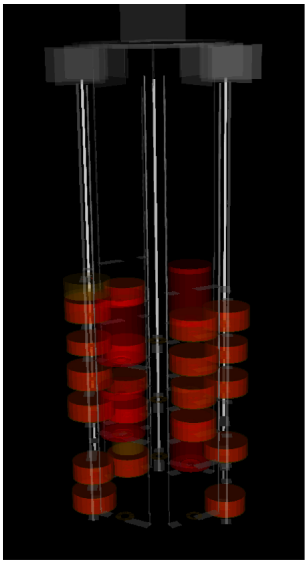

Figure 12: The GERDA setup of the detector array in Geant4. The red disks represent the germanium detectors. The figure is taken from [7].

4.2 Running Simulations

In the first step, 5×10^6 decays of ^{75}Ge are generated in a single detector. This is done for all the 30 BEGe detectors and all the 10 coaxial detectors. Afterwards, the simulation output is post processed to retrieve the event energy distribution. The 265 keV gamma coincidence events in neighbouring detectors

are then identified and used to calculate the efficiency between each pair of detectors.

4.2.1 Vertex Position in Germanium Detector

The events generated in the germanium detectors are uniformly distributed as shown in Figure 13.

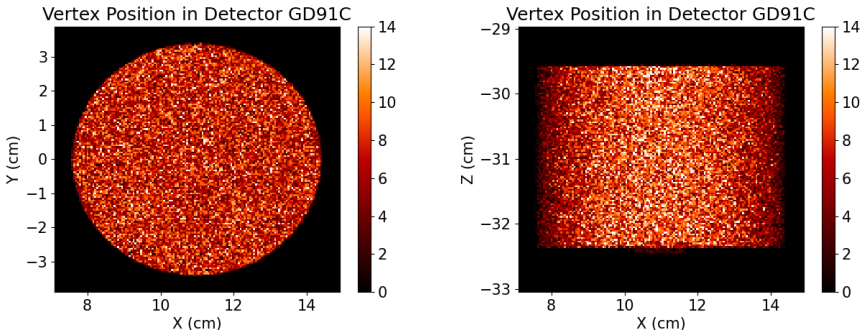

(a) Top view (b) Side view

Figure 13: Vertex position in the BEGe detector GD91C (ID 7). The color indicates the number of vertices.

4.2.2 Hit Distribution in Germanium Detectors and in Liquid Argon

The gammas emitted after the β decay do not always stay in the source detector. Some may escape the detector where the decay happened, pass through the liquid argon and enter a neighbouring detector. As examples, Geant4 simulations of neutron disappearance events in a BEGe detector (GD00D) and in a coaxial detector (GTF45), respectively, are run. Figure 14 and Figure 15 show the corresponding hit distribution in germanium detectors and in liquid argon, respectively.

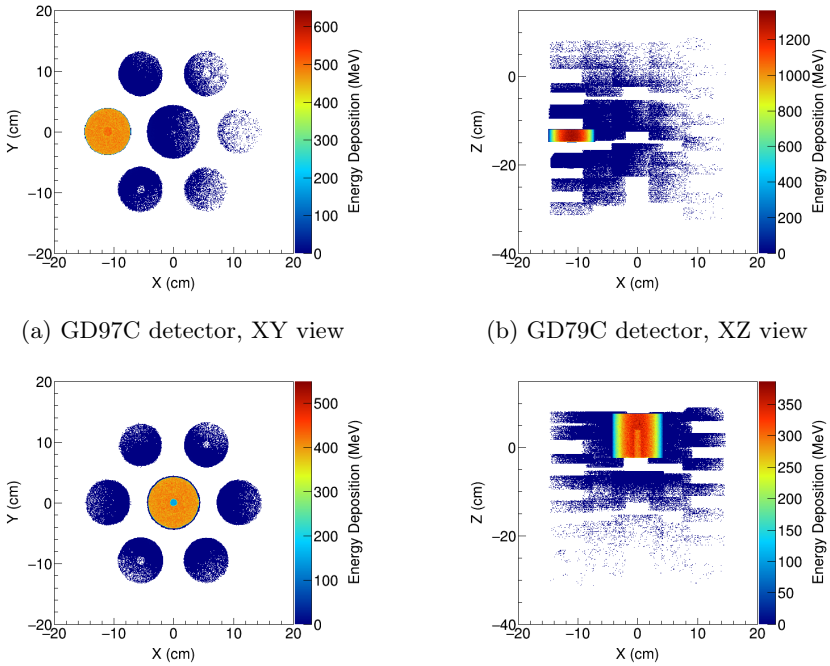

(a) GD97C detector, XY view

(b) GD79C detector, XZ view

(c) GTF45 detector, XY view

(d) GTF45 detector, XZ view

Figure 14: Hit distribution in germanium detectors. 5×10^6 events are generated in a BEGe detector (plots (a) and (b)) and in a coaxial detector (plots (c) and (d)), respectively. The color represents the energy distribution in the germanium detectors.

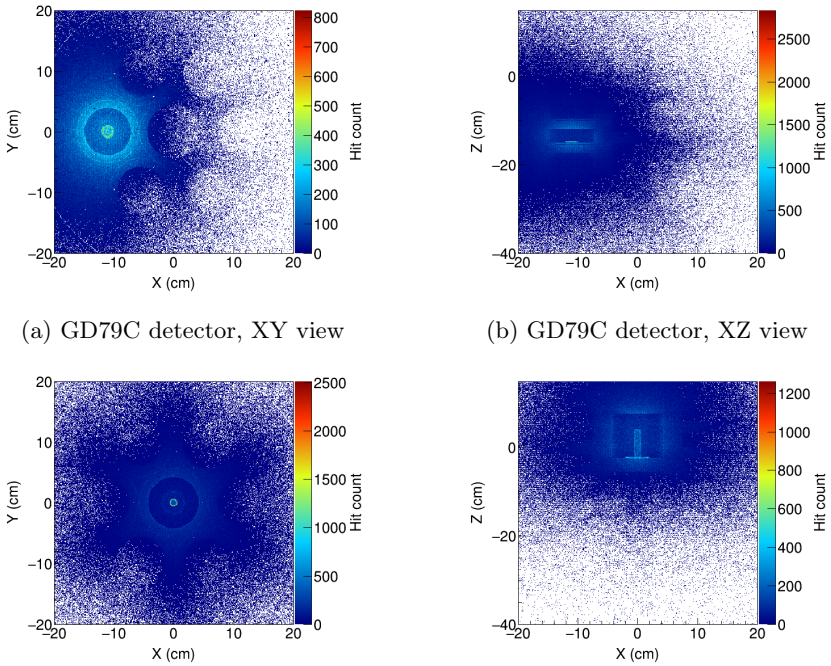

(a) GD79C detector, XY view

(b) GD79C detector, XZ view

(c) GTF45 detector, XY view

(d) GTF45 detector, XZ position

Figure 15: Hit distribution in liquid argon due to the decays of ^{75}Ge in a germanium detector. 5M events are generated in a BEGe detector (plots (a) and (b)) and in a coaxial detector (plots (c) and (d)), respectively. The color represents the hit distribution in liquid argon.

The BEGe detector GD79C was selected because it is in the middle of a string. To show the influence of events generated in a detector located on the string in the centre, the coaxial detector GTF45 was selected.

The hit distribution in germanium detectors (Figure 14) indicates that the number of detected gammas is, apart from the source detector, highest in neighbouring detectors and decreases with increasing distance from the source detector. This correlation between detector efficiency and detector location holds true for both the BEGe and the coaxial detectors.

4.3 Efficiency Calculations

4.3.1 Energy Spectra - Possible Signatures in GERDA

An example of the energy spectra at the source detector and at all the neighbouring detectors are presented in Figure 16. In the source detector, the combined energy of the electron and the gammas is measured. The neighbouring detectors

measure only the energy of the gammas.

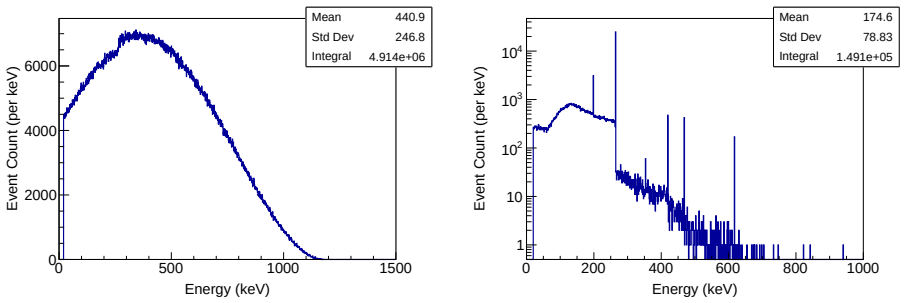

(a) Source detector (GD02B) (b) All the neighbouring detectors

Figure 16: Energy spectra at the source detector (GD02B) and at all the neighbouring detectors. The energy threshold is set to 20 keV

.

Figure 16a shows the energy spectrum of the simulated β decay of ^{75}Ge to stable ^{75}As seen by the source detector. It ends around 1.2 MeV, which coincides with the measured β decay energy presented in Figure 11.
Looking at the energy spectrum of all the neighbouring detectors in Figure 16b, the most significant peak is at 265 keV. Thus, the 265 keV can be used as the signature of the neutron disappearance from ^{76}Ge.

4.3.2 Signal Efficiency

The efficiencies between detectors are calculated by dividing the number of observed 265 keV gammas in the detector by the total number of events (5×10^6 events in this study). Figure 17 presents the signal efficiencies between each pair of the detectors. The events were generated in the detectors shown on the x-axis.
The corresponding numbers are listed in Table 7 in the appendix.

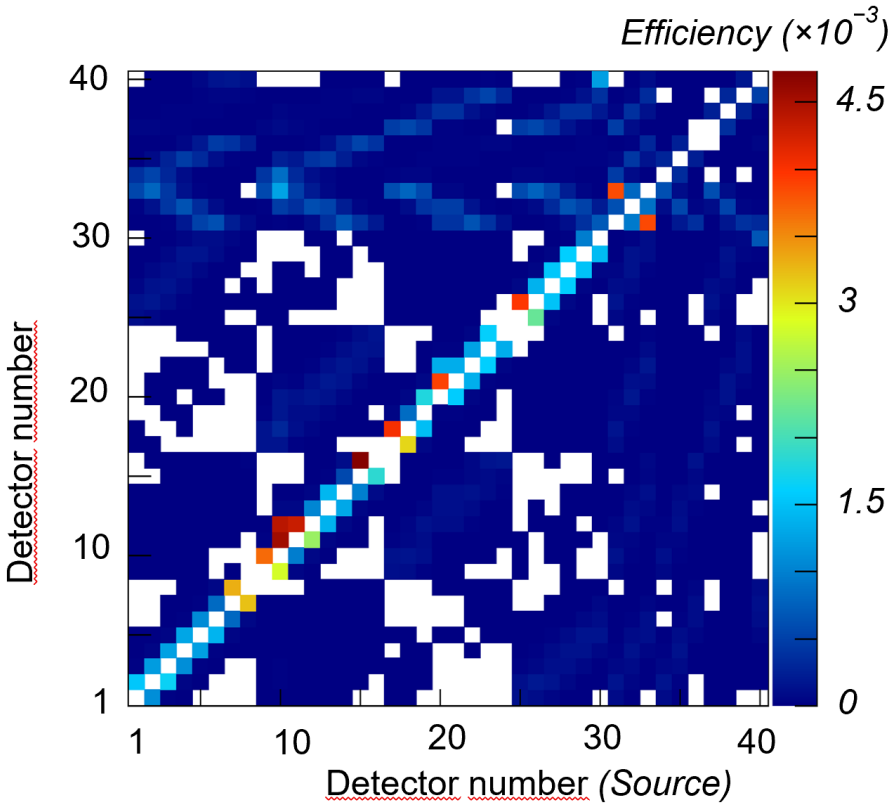

Figure 17: Efficiency of detecting 265 keV gammas in the neighbouring detectors. Detector numbers 1 to 30 correspond to BEGe detectors, 31 to 40 correspond to coaxial detectors.

To clearly show the difference in coaxial and BEGe detectors, the detectors are numbered such that Nr. 1 to 30 correspond to BEGe detectors, Nr. 31 to 40 represent coaxial detectors. This labeling differs from the detector ID used in the later data analysis.

For the interpretation of the results presented in Figure 17, the map of the spatial arrangement of the germanium detectors (see Figure 8) as well as Table 2 below are useful.

Nr.	Name	Active Mass (kg)	Nr.	Name	Active Mass (kg)	Nr.	Name	Active Mass (kg)
1	GD91A	0.557	15	GD76B	0.326	29	GD32D	0.657
2	GD35B	0.740	16	GD00C	0.727	30	GD89A	0.462
3	GD02B	0.553	17	GD35C	0.572	31	GTF45	1.965
4	GD00B	0.613	18	GD76C	0.723	32	GTF32	2.251
5	GD61A	0.652	19	GD89D	0.454	33	GTF112	2.522
6	GD89B	0.533	20	GD00D	0.723	34	ANG5	2.281
7	GD02D	0.552	21	GD79C	0.713	35	RG1	1.908
8	GD91C	0.556	22	GD35A	0.693	36	ANG3	2.070
9	GD02A	0.488	23	GD91B	0.578	37	ANG2	2.468
10	GD32B	0.632	24	GD61B	0.666	38	RG2	1.800
11	GD32A	0.404	25	GD00A	0.439	39	ANG4	2.136
12	GD32C	0.665	26	GD02C	0.700	40	ANG1	0.795
13	GD89C	0.520	27	GD79B	0.648			
14	GD61C	0.562	28	GD91D	0.615			

Table 2: Detector number, corresponding detector name and active mass in kg.

In general, the efficiency between neighbouring detectors is better than between detectors that are further away. This is expected, based on the results of the hit distribution in germanium detectors. For example, detector GD89B (Nr. 6) and detector GD02D (Nr. 7) are further away from each other than detector GD02D (Nr. 7) and detector GD91C (Nr. 8), leading to a smaller signal efficiency.

One might expect a symmetric pattern for the signal efficiency between the detectors, however, the results show a different picture. Apart from some minor deviations which stem from statistical fluctuations, the main explanation for this asymmetry comes from the difference in detector size, and thus in active mass, between the BEGe and the coaxial detectors. The latter are more than twice as large as the first ones. The efficiency is larger, if events are generated in a BEGe detector and 265 keV gammas are detected by a coaxial detector than vice versa. The effect can be seen in the upper quarter of Figure 17, where there is a pattern of diagonals. Here, the events are generated in BEGe detectors. In the lower quarter on the right, corresponding to the reversed situation, the pattern is not visible. Not only the difference in size between the detector types plays a role but also the difference in size between detectors of the same type is important when considering adjacent detectors. The asymmetry between the BEGe detector pairs GD02A|GD32B (Nr. 9|10), GD32A|GD32C (Nr. 11|12), GD76B|GD00C (Nr. 15|16), GD35C|GD76C (Nr. 17|18), GD89D|GD00D (Nr. 19|20) and GD00A|GD02C (Nr. 25|26) can be explained by the difference in size and in active mass. Events generated in the firstly mentioned detector leads to a higher efficiency due to the fact that the secondly mentioned detector is larger. However, there is one detector pair that contradicts this correlation, namely the pair GD32B|GD32A (Nr. 10|11). Events generated in detector 10 lead to a higher efficiency, although detector 11 is smaller in size. One possible explanation for this anomaly could stem from the relative orientation of the

detectors, where the p+ electrodes of the detectors face each other. The same relative orientation is found between the detector pairs GD89B|GD02D (Nr. 6|7) and GD61C|GD76B (Nr. 14|15), that both show no asymmetry in signal efficiency. However, it has to be pointed out that detectors GD89B (Nr. 6), GD02D (Nr. 7) and GD76B (Nr. 15) are passivated, meaning that the current flowing between n+ and p+ electrodes is reduced, whereas detectors GD32B and GD32A (Nr. 10 and 11) are not. Therefore, a direct comparison between the pairs may not be very informative.
The asymmetry in signal efficiency between the detector pairs GD32B|GD32C (Nr. 10|12) and GD00D|GD79C (Nr. 20|21), where both detectors have roughly the same active mass, is not understood yet.

The white spots off the diagonal indicate that there is no event available for the calculation of the signal efficiency between the detector pair. This is often the case for detectors located on different strings. More simulations would need to be run to get some events in those detectors.

4.4 Signal Efficiency Calculation

To determine the efficiency of detecting 265 keV gammas, a simple approach was applied. A more elaborate approach has been developed simultaneously but due to time restrictions, this approach has not yet been applied. It is briefly discussed in section 7.

In this approach, only a mean efficiency is calculated for all detectors. The following formula for the mean is applied

$$\bar{\epsilon} = \frac{1}{N} \sum_{i=1}^{N} \epsilon_i \tag{1}$$

where N is the number of detectors and ϵ_i corresponds to the sum of efficiencies between detector i and all the other detectors, listed in Table 7. Applying Eq. 1, an average efficiency of 0.48% is obtained.
The systematic uncertainty stems from the inaccuracy of the simulation and is conservatively estimated at 5%. For the estimation of the statistical uncertainty, the following formula is used

$$\sigma_{stat.} \approx \frac{1}{\sqrt{\bar{\epsilon} \cdot n}} = \frac{1}{24 \times 10^3} = 0.6\%, \tag{2}$$

where $\bar{\epsilon}$ is the arithmetic mean of the efficiency and n is the number of events, in this case 5×10^6.
In summary, the simple approach leads to an average 265 keV gamma detection efficiency of 0.48% with an uncertainty of

$$\sigma = \sqrt{\sigma_{syst.}^2 + \sigma_{stat.}^2} = 5.04\% \tag{3}$$

on the 0.48%. The β decay tagging efficiency is discussed together with the exposure in chapter 5.

5 Data Analysis

This chapter discusses the analysis of GERDA data taken in runs 53 to 93 of Phase II before the 2018 upgrade. A summary of the runs taken in GERDA Phase II is presented in Table 3. The aim of the data analysis is to perform an event selection in order to obtain the candidate event count which will be used in the statistical analysis.

Upgrade	Threshold	Run	Excluded runs	Run count	Date
before	150 keV	53–86	66, 68, 80–82	29	Dec. 2015 – Oct. 2017
	16 keV	87–93	N/A	7	Oct. 2017 – Apr. 2018
after	16 keV	95–114	102	19	May 2018 – Nov. 2019

Table 3: Summary of the runs taken in GERDA Phase II.

5.1 Exposure

The exposure λ is defined as follows

$$\lambda = m_{active} \times f \times t \times \epsilon_\beta \tag{4}$$

where m_{active} is the active mass, f is the enrichment in ^{76}Ge, t is the running time and ϵ_β is the single β decay efficiency. As no detailed studies were performed on the latter, the $0\nu\beta\beta$ detection efficiency is used as an approximation. It contains the LAr veto, the electron containment and the pulse shape discrimination (PSD) and has an average value of 88%. For detailed numbers refer to [18].
For the understanding of this study it would have been clearer to separate the β decay efficiency from the exposure. However, since the β decay efficiency varies detector by detector, a higher accuracy is reached by using the product compared to taking an average β decay efficiency.

A summary of the ^{76}Ge exposure from run 53 to run 93 is illustrated in Figure 18. In total, the ^{76}Ge exposure during this period is 41.58 kg year. An uncertainty of 10% is estimated based on the uncertainties used in [18].

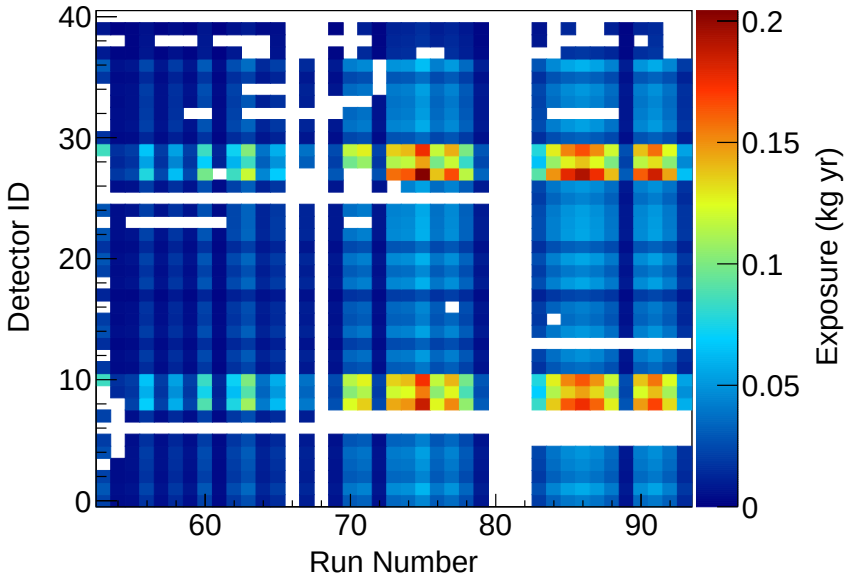

Figure 18: Exposure per detector per run in kg year.

5.2 Event Selection

For the physics analysis, only data taken during stable operating conditions are used. This corresponds to about 80% of the total [20]. Several cuts, described in the sections below, are then applied to the data to select candidate events.

Veto Cuts
The cosmic ray veto rejects events from cosmic muons depositing energy in either the water tank or plastic scintillation panels [20]. Events depositing energy in liquid argon within 5 µs from the germanium signal are rejected as background events by the liquid argon veto [22]. Additionally, test pulser and baseline events are excluded as well as detectors that are off or not part of the data set [28].

Multiplicity Cut
A further selection criterion is the multiplicity. Only events of double coincidence between two detectors, one of which sees an energy between 255 keV and 275 keV, are considered. This corresponds to multiplicity 2 in Figure 19. In total, 395 events of double coincidence were found.

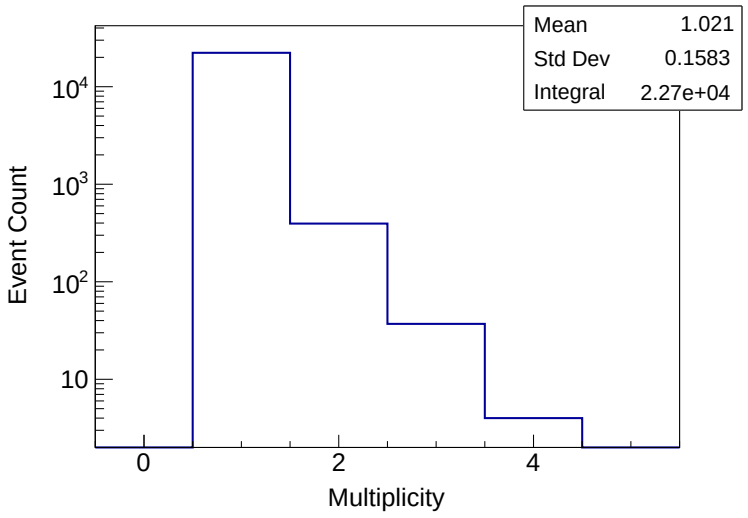

Figure 19: Multiplicity of events after the veto cuts.

265 keV Gamma Energy Cut
Since the 265 keV gammas are of interest for this study, it is required that in at least one of the detectors the energy is in a 3σ interval around 265 keV, where σ is the energy resolution of the detector. To determine σ, the proportionality to the full width at half maximum (FWHM) is used. A semi-empirical formula is used to express the FWHM as a function of the energy,

$$\text{FWHM} = 2.355\sigma = 2.355\sqrt{a + bE}, \tag{5}$$

where E is the energy and a and b are fit parameters that depend on the detector type [20]. The latter are obtained from the calibration data and are listed in Table 4. Figure 20 shows the resolution curves of the BEGe and coaxial detectors.

Detector type	a [keV^2]	b [10^{-4} keV]	FWHM at 265 keV [keV]
BEGe	0.681 ± 0.001	4.27 ± 0.01	2.081 ± 0.001
Coaxial	1.025 ± 0.002	6.47 ± 0.02	2.554 ± 0.002

Table 4: Parameters and errors of Eq. 5 for the pre 2018 upgrade period of Phase II. Table adapted from [20].

To estimate the uncertainty on the FWHM at 265 keV, error propagation is applied.

$$\sigma_{FWHM,\ 265keV} = 2.355 \cdot \frac{1}{2\sqrt{a + b \cdot 265}} \cdot \sqrt{\sigma_a^2 + (265)^2\sigma_b^2} \tag{6}$$

where $\sigma_{FWHM,\ 265keV}$ is the uncertainty on the FWHM at 265 keV, σ_a is the uncertainty on parameter a and σ_b is the uncertainty on parameter b.

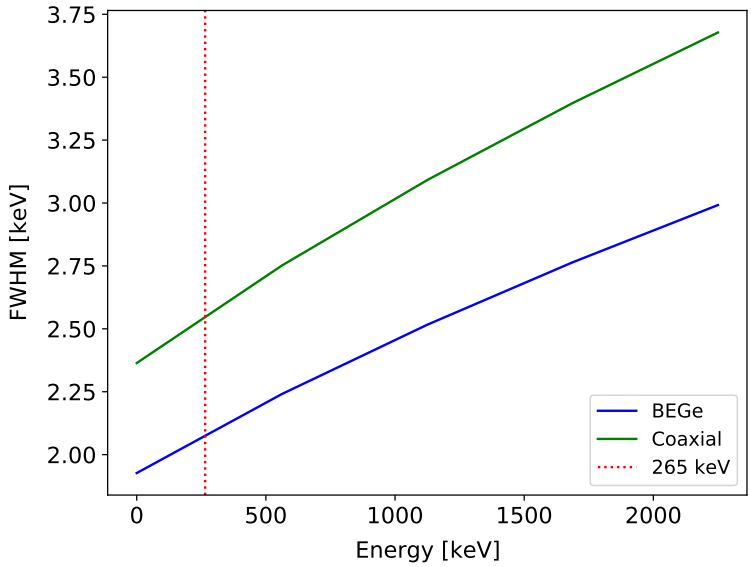

Figure 20: Resolution curves of BEGe and coaxial detectors at low energies before the Phase II upgrade.

The application of Eq. 5 and Table 4 to lower energies is verified by [29] using a special calibration run with a low threshold. As can be seen in Figure 21, the discrepancy between the measured FWHM and the result from the fit of the resolution curve is small ($< 1\%$ or $\sim 1\%$) [29].

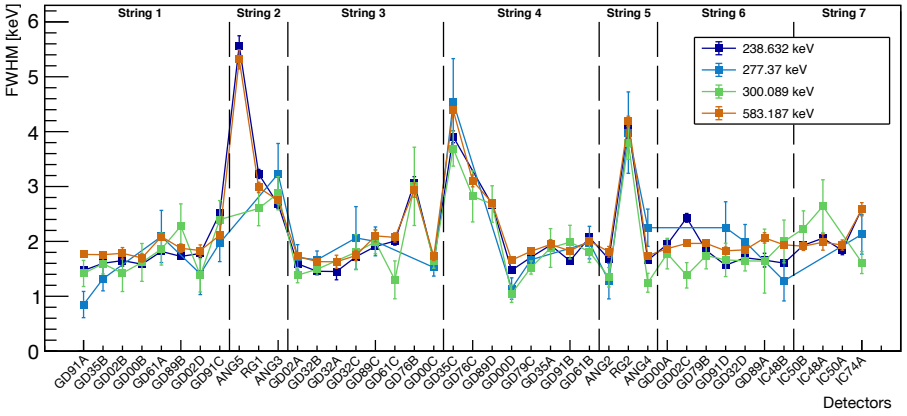

(a) FWHM of all the detectors

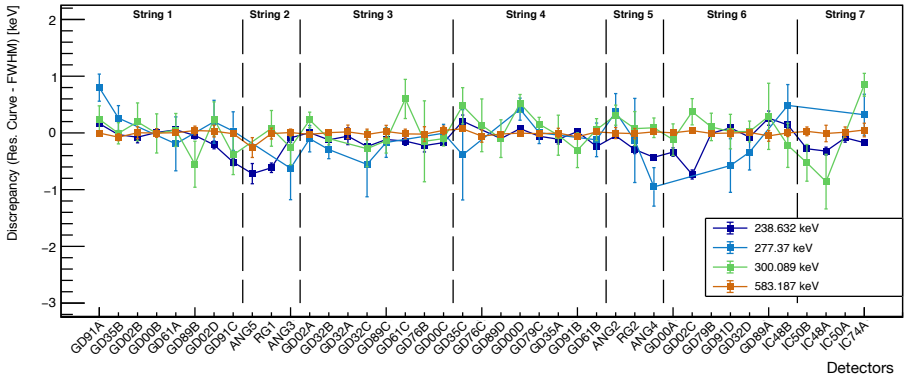

(b) Discrepancy of all the detectors

Figure 21: The resolution of low energy peaks for all detectors. The y-axis corresponds to (a) the measured FWHM itself and (b) the discrepancy between the FWHM based on the resolution curve and the measured FWHM. The figures are taken from [29].

The event count per keV for an energy window of 255 keV - 275 keV and the event count per keV for an energy window of 3σ around 265 keV are illustrated in Figure 22.
Figure 22b has a peak structure, leading to the suspicion that there is a signal. However, by selecting a wider energy window around 265 keV as shown in Figure 22a, one sees that the peak at 265 keV is not significant compared to the neighbouring peaks but rather statistical fluctuations.

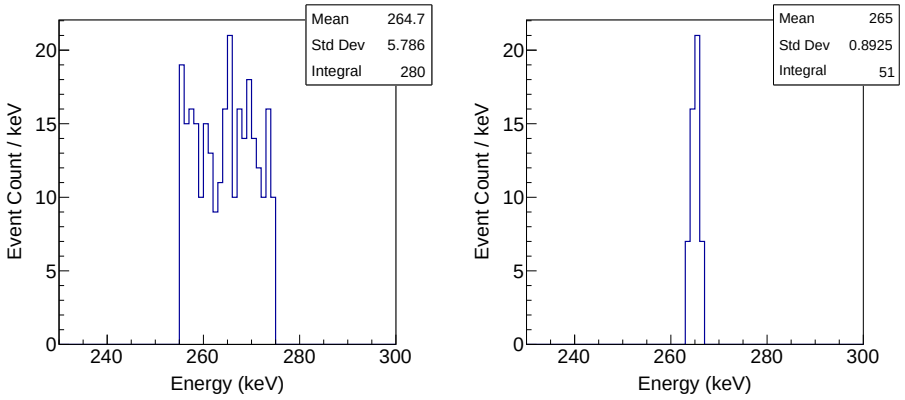

(a) 255 keV - 275 keV energy window (b) 3σ energy window

Figure 22: Event count per keV for different energy windows around 265 keV.

Beta Decay Cuts

A cut on the maximum β decay energy $Q = 919\,\text{keV}$ is applied. This corresponds to the β decay marked in green in Figure 11. Only events with energies smaller than the Q value of the β decay are considered.

β decays are always single-site events (SSE) whereas gammas can either be SSE or they can interact with the detector multiple times, referred to as multi-site events (MSE). The different types of events can be identified via their pulse shape, as illustrated in Figure 23. Thus, in addition to the energy cut, a pulse shape discrimination (PSD) cut is applied to select β decays. To illustrate the effect of the PSD cut, Figure 24b shows the energies of the β decays without a PSD cut. 43 events have energies smaller than the Q value of the β decay compared to 34 events with the PSD cut applied, shown in Figure 24a.

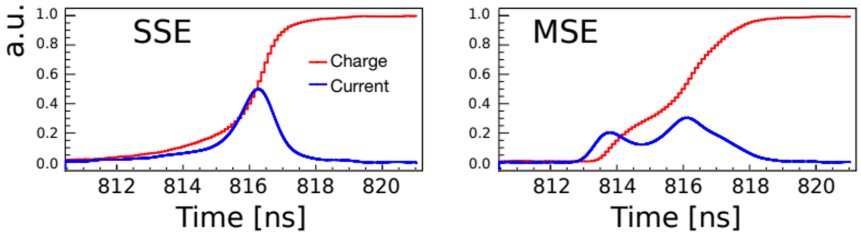

Figure 23: Examples of the charge and current wave forms for various types of events of the same energy. By the shape of the charge and current pulses, the PSD algorithms identify signal-like events (SSE) from MSE events. The figure is taken from [30].

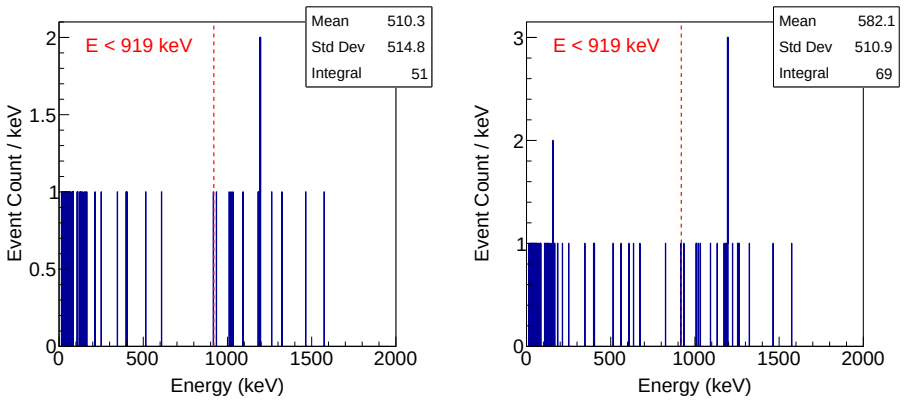

(a) with PSD cut (b) without PSD cut

Figure 24: The cut on the maximum β decay energy of Q = 919 keV is indicated in red.

In total, 34 events satisfy all the data selection criteria for data from run 53 to 93.

6 Statistical Analysis

This chapter presents the statistical analysis that was done to place a constraint on the lifetime limit of neutron disappearance in ^{76}Ge.
The statistical method used in this thesis is similar to the one applied in the search for $n - \bar{n}$ oscillation in Super-Kamiokande [9].

6.1 Poisson Statistics

To answer the question of how many events will be observed in a time interval T, Poisson distribution is applied. Given the number of expected events n_{exp}, the probability of observing n_{obs} events is

$$P(n_{obs}|n_{exp}) = \frac{e^{-n_{exp}} \cdot n_{exp}^{n_{obs}}}{n_{obs}!}. \tag{7}$$

For a decay with lifetime τ, the number of expected events is

$$n = N(1 - e^{-t/\tau}) \approx Nt/\tau \tag{8}$$

where N is the initial number of neutrons and t is the observation time assuming $t \ll \tau$.
The event rate Γ is defined as the fraction of decayed particles per unit time:

$$\Gamma \equiv \left(\frac{n}{N}\right)\frac{1}{t} = \frac{n}{\lambda}, \tag{9}$$

where $\lambda \equiv Nt$ is the exposure. It follows that

$$\tau = \frac{1}{\Gamma}, \tag{10}$$

$$n = \Gamma\lambda. \tag{11}$$

Considering the signal efficiency ϵ and the total number of expected background events b, the total number of expected events is calculated as

$$n_{exp} = \Gamma\lambda\epsilon + b \tag{12}$$

Thus, Eq. 7 becomes

$$P(n_{obs}|n_{exp}) = \frac{e^{-(\Gamma\lambda\epsilon+b)} \cdot (\Gamma\lambda\epsilon + b)^{n_{obs}}}{n_{obs}!}. \tag{13}$$

The information for this section is taken from [31].

6.2 Bayes' Theorem

In order to include all of the systematic uncertainties in the limit calculation, Bayesian statistics is applied. Bayes' theorem states that

$$P(A|B)P(B) = P(B|A)P(A) \text{ or } P(A|B) = \frac{P(B|A)P(A)}{P(B)} \tag{14}$$

where $P(B) = P(A)P(B|A) + P(\bar{A})P(B|\bar{A})$. This can be applied to the case of data and model parameters as follows

$$P(parameter|data) = \frac{P(data|parameter)P(parameter)}{P(data)} \tag{15}$$

where $P(parameter|data)$ is the posterior probability, $P(data|parameter)$ is the likelihood, $P(data)$ is the evidence and $P(parameter)$ is the prior probability [32].

6.2.1 Application to the GERDA Experiment

The probability of the expected number of events n_{exp}, given n_{obs} observed events is

$$P(n_{exp}|n_{obs})dn_{exp} \tag{16}$$

where $P(n_{exp}|n_{obs})$ is a probability density function.
Employing Bayes' theorem stated in Eq. 14 leads to

$$P(n_{exp}|n_{obs})dn_{exp} = P(n_{obs}|n_{exp})P(n_{exp})dn_{exp} \tag{17}$$

where $P(n_{obs}|n_{exp})$ and $P(n_{exp})$ are probability density functions.
Since n_{exp} is a function of $\Gamma, \lambda, \epsilon$ and b, the probability $P(n_{exp})dn_{exp}$ that the expected number of events is n_{exp} becomes

$$P(n_{exp})dn_{exp} = [P(\Gamma)d\Gamma][P(\lambda)d\lambda][P(\epsilon)d\epsilon][P(b)db] \tag{18}$$

where $P(x)$ for $x = \Gamma, \lambda, \epsilon$,b are the probability density functions.
By inserting Eq. 18 into Bayes' theorem Eq. 17 it follows

$$P(n_{exp}|n_{obs})d\Gamma d\lambda d\epsilon db = P(n_{obs}|n_{exp})[P(\Gamma)d\Gamma][P(\lambda)d\lambda][P(\epsilon)d\epsilon][P(b)db]. \tag{19}$$

Of interest for the statistical analysis is the probability of the event rate Γ given the number of observed events n_{obs}. This probability is calculated by summing up contributions to the range of Γ to $\Gamma + d\Gamma$ from all $d\lambda, d\epsilon$ and db, following in

$$P(\Gamma|n_{obs})d\Gamma = A \iiint P(n_{exp}|n_{obs})\, d\Gamma\, d\lambda\, d\epsilon\, db \tag{20}$$

where A is the normalisation constant, determined by imposing the constraint

$$\int_0^\infty P(\Gamma|n_{obs})\, d\Gamma = 1. \tag{21}$$

Employing Eq. 19 and dropping $d\Gamma$ on both sides leads to

$$P(\Gamma|n_{obs}) = A \iiint P(n_{obs}|n_{exp})P(\Gamma)P(\lambda)P(\epsilon)P(b)\, d\lambda\, d\epsilon\, db. \tag{22}$$

Inserting the Poisson distribution from Eq. 13, it follows

$$P(\Gamma|n_{obs}) = A \iiint \frac{e^{-(\Gamma\lambda\epsilon+b)}(\Gamma\lambda\epsilon+b)^{n_{obs}}}{n_{obs}!} \times P(\Gamma)P(\lambda)P(\epsilon)P(b)\, d\lambda\, d\epsilon\, db \tag{23}$$

The probability density function for the decay rate $P(\Gamma)$ is taken to be flat, whereas the probability density functions for the exposure $P(\lambda)$ and for the efficiency $P(\epsilon)$ are assumed to be Gaussian distributions. To obtain the most conservative limit on Γ, the background b is set to zero and will be further discussed in section 6.4.
The information for this section is taken from [31].

6.3 Numerical Integration - The Midpoint Rule

The integrals appearing in Eq. 23 are solved numerically by applying the midpoint rule. This method is based on the concept of the Riemann sum. The idea is to approximate the area under the graph by dividing it into rectangles and summing up their area.

The Midpoint Rule
Let $f(x)$ be continuous on a closed interval [a,b] that is subdivided into n subintervals of equal length $\Delta x = (b-a)/n$. This gives $n+1$ points $x_i = a + i\Delta x$, where $i = 0, 1, ..., n$:

$$x_0 = a, x_1 = a + \Delta x, ..., x_{n-1} = a + (n-1)\Delta x, x_n = b \tag{24}$$

The integral $\int_a^b f(x)dx$ can then be approximated by

$$\int_a^b f(x)dx \approx \sum_{i=1}^{n} f\left(\frac{x_{i-1} + x_i}{2}\right)\Delta x \tag{25}$$

The cost of the simplicity of the midpoint rule is the large number of rectangles needed to get acceptable accuracy [33].

For the integration over Γ, λ and ϵ, 10 rectangles have been used for each.

6.4 Results

The parameters with their uncertainties used for the statistical analysis are presented in Table 5.

Parameter		Value	Uncertainty (%)
Exposure × Beta tagging efficiency	λ	41.58 kg year	10
265 keV gamma tagging efficiency	ϵ	0.48 %	5.04
Background rate	b	0	0
Observed events	n_{obs}	34 events	N/A

Table 5: Parameters and their uncertainties used for the statistical analysis of GERDA data. The signal efficiency ϵ is taken from the results of the MaGe simulation. The exposure λ is taken from chapter 5.1. The uncertainty is used to give the width to the Gaussian distribution assumed for λ, ϵ and b.

Since the unit of the exposure is kg year but Eq. 23 requires the unit of neutron year, a conversion has to be undertaken.

$$\lambda_{\text{neutron yr}} = n \cdot \frac{\lambda_{\text{kg yr}}}{M} \cdot N_A = 44 \cdot \frac{41.58\,\text{kg yr}}{76\,\text{g/mol}} \cdot 6.02 \times 10^{23}\,\text{mol}^{-1} = 1.45 \times 10^{28}\,\text{neutron yr} \tag{26}$$

where $n = 44$ is the number of neutrons in ^{76}Ge, $M = 76\,\text{g/mol}$ is the molar mass and N_A is the Avogadro constant.

Plugging the values from Table 5 and Eq. 26 into Eq. 23 leads to the probability density function presented in Figure 25.

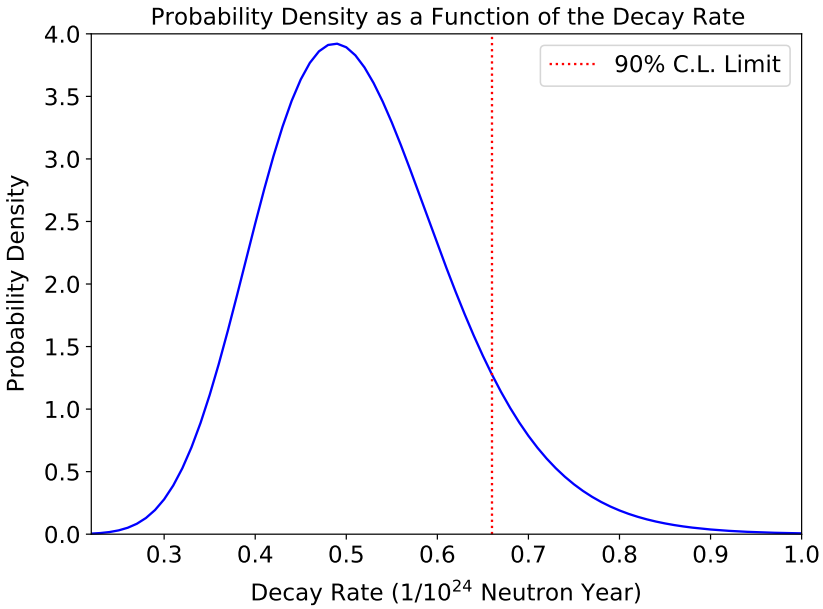

Figure 25: The probability density as a function of the decay rate. The limit on the decay rate at 90% C.L. is indicated with the red dotted line.

The 90% confidence level is determined as follows

$$C.L. = \int_0^{\Gamma_{limit}} P(\Gamma|n)\, d\Gamma = 0.9. \tag{27}$$

As shown in Figure 25, the 90% C.L. limit on the decay rate is $\Gamma > 0.66 \times 10^{-24}$ neutron year.
The calculated result on the lifetime limit, corresponding to the inverse of the limit on the decay rate, is

$$\tau > 1.5 \times 10^{24}\,\text{year at } 90\%\text{ C.L.} \tag{28}$$

The inequality stems from the fact that the signal event count must be smaller than the selected number of events.

6.4.1 Effect of the Background on the Limit

The distribution of the expected background has a significant effect on the limit on the decay rate. To illustrate this, three different scenarios for the background are implemented in Eq. 23: a Gaussian distribution, a flat distribution and no background. For the Gaussian distribution, the mean is set to $\mu = 34$ events and the standard deviation is 20% of the mean. The choice is based on the number of observed events, set to $n_{obs} = 34$. The flat distribution is normalised and returns the value $1/100$ for the background between 0 and 100 and is zero everywhere else. The exposure and the efficiency with their uncertainties are taken from Table 5. Figure 26 presents the influence on the shape of the probability density function and on the limit as graphs. The numerical results on the limit are summarized in Table 6.

Background distribution	$\Gamma_{90\%}$ $(1/10^{24}$ neutron year)
Gaussian	0.25
Flat	0.49
No background	0.66

Table 6: Influence of different background distributions on the limit on the decay rate Γ at 90% confidence level.

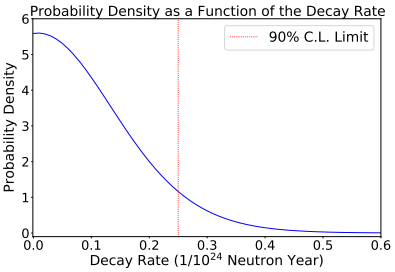

(a) Gaussian distribution for background

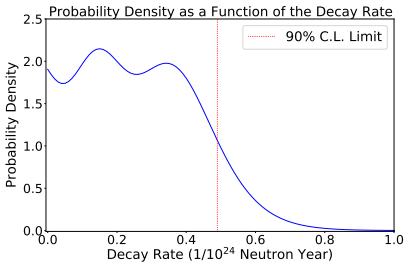

(b) Flat distribution for background

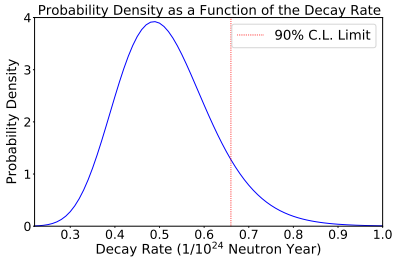

(c) No background

Figure 26: Different scenarios for the distribution of the background events.

As can be seen in Figure 26, the probability density function transforms from an exponential function (a) to a Gaussian shaped function (c). At the same time, the limit on the decay rate is increasing, becoming more conservative. Since no study on the background sources has been conducted, the background for the statistical analysis in this thesis is set to zero. This leads to the most conservative limit on the decay rate.

7 Conclusion and Outlook

The aim of this thesis was to set a limit on the lifetime of single neutron disappearance in ^{76}Ge using GERDA Phase II data before the 2018 upgrade. With the results from the simulation and the data analysis, a limit of $\tau > 1.5 \times 10^{24}$ year at 90% C.L. has been obtained. Compared to the results of previous single neutron decay searches (Table 1 of chapter 1), the obtained limit is by 5 orders smaller. However, previous searches have only been conducted for ^{16}O and ^{12}C nuclei. This work is the first search with ^{75}Ge.

In a next step, a more detailed efficiency study should be conducted to improve the limit estimation on the lifetime. A more rigorous approach based on the run configurations has already been worked on. The idea is to calculate the efficiency and exposure for each run separately.
Additionally, the data after the 2018 upgrade, accounting for 40% of the total Phase II data, should also be included in the analysis.
Finally, a background study should be conducted to better understand the background signals. This would allow a less conservative limit estimation.

A nextgeneration germanium experiment is LEGEND (Large Enriched Germanium Experiment for Neutrinoless $\beta\beta$ Decay), which combines the technological expertise and experience from GERDA and Majorana Demonstrator. LEGEND-200 aims for an exposure of 1 t year and will start taking data at the end of this year [34]. Due to the large exposure ($\sim$ 10 times more than GERDA), the estimated limit on the lifetime of single neutron disappearance is expected to improve.
Other current and upcoming large-scale experiments of significance for the search of nucleon disappearance are Super-Kamiokande, Hyper-Kamiokande, JUNO (Jiangmen Underground Neutrino Observatory) and DUNE (Deep Underground Neutrino Experiment). The first two experiments are expected to provide the furthest reach in sensitivity due to their unparalleled size. The latter two experiments are promising, since their low-energy sensitivity could be particularly beneficial for nuclear de-excitation emission searches, e.g. invisible decay channels [2].

References

[1]J. C. Pati and A. Salam, "Unified Lepton-Hadron Symmetry and a Gauge Theory of the Basic Interactions", Phys. Rev. D **8**, 1240–1251 (1973).

[2]J. Heeck and V. Takhistov, "Inclusive Nucleon Decay Searches as a Frontier of Baryon Number Violation", Phys. Rev. D **101**, 015005 (2020).

[3]Y. A. Kamyshkov and E. Kolbe, "Signatures of nucleon disappearance in large underground detectors", Phys. Rev. D **67**, 076007 (2003).

[4]P. A. Zyla et al. (Particle Data Group), "Review of Particle Physics", PTEP **2020**, 083C01 (2020).

[5]B. Fornal and B. Grinstein, "Dark Side of the Neutron?", EPJ Web Conf. **219**, edited by T. Jenke, S. Degenkolb, P. Geltenbort, M. Jentschel, V. V. Nesvizhevsky, D. Rebreyend, S. Roccia, T. Soldner, A. Stutz, and O. Zimmer, 05005 (2019).

[6]S. Weinberg, *The First Three Minutes. A Modern View of the Origin of the Universe* (1977), 269p.

[7]J. Huang, "Lepton and baryon number violation searches with high purity germanium detectors", Internal report, (2020).

[8]A. D. Sakharov, "Violation of CP Invariance, C asymmetry, and baryon asymmetry of the universe", Pisma Zh. Eksp. Teor. Fiz. **5**, 32–35 (1967).

[9]K. Abe et al. (Super-Kamiokande), "The Search for $n-\bar{n}$ oscillation in Super-Kamiokande I", Phys. Rev. D **91**, 072006 (2015).

[10]B. Fornal and B. Grinstein, "Dark Matter Interpretation of the Neutron Decay Anomaly", Phys. Rev. Lett. **120**, [Erratum: Phys.Rev.Lett. 124, 219901 (2020)], 191801 (2018).

[11]J. Boger et al. (SNO), "The Sudbury neutrino observatory", Nucl. Instrum. Meth. A **449**, 172–207 (2000).

[12]S. N. Ahmed et al. (SNO), "Constraints on nucleon decay via 'invisible' modes from the Sudbury Neutrino Observatory", Phys. Rev. Lett. **92**, 102004 (2004).

[13]S. Abe et al. (KamLAND), "Precision Measurement of Neutrino Oscillation Parameters with KamLAND", Phys. Rev. Lett. **100**, 221803 (2008).

[14]T. Araki et al. (KamLAND), "Search for the invisible decay of neutrons with KamLAND", Phys. Rev. Lett. **96**, 101802 (2006).

[15]V. Albanese et al. (SNO+), "The SNO+ Experiment", (2021).

[16]M. Anderson et al. (SNO+), "Search for invisible modes of nucleon decay in water with the SNO+ detector", Phys. Rev. D **99**, 032008 (2019).

[17]S. I. Alvis et al. (Majorana), "Search for trinucleon decay in the Majorana Demonstrator", Phys. Rev. D **99**, 072004 (2019).

[18]M. Agostini et al. (GERDA), "Final Results of GERDA on the Search for Neutrinoless Double-β Decay", Phys. Rev. Lett. **125**, 252502 (2020).

[19]LNGS, *Gerda*, `https://www.lngs.infn.it/en/gerda`, (accessed: 15.07.2021).

[20]C. Ransom, "Energy Calibration for the GERDA and LEGEND-200 Experiments", PhD thesis (University of Zurich, 2021).

[21]K. H. Ackermann et al. (GERDA), "The GERDA experiment for the search of $0\nu\beta\beta$ decay in ^{76}Ge", Eur. Phys. J. C **73**, 2330 (2013).

[22]M. Agostini et al. (GERDA), "Searching for neutrinoless double beta decay with GERDA", J. Phys. Conf. Ser. **1342**, edited by K. Clark, C. Jillings, C. Kraus, J. Saffin, and S. Scorza, 012005 (2020).

[23]N. Abgrall et al. (LEGEND), "The Large Enriched Germanium Experiment for Neutrinoless $\beta\beta$ Decay: LEGEND-1000 Preconceptual Design Report", (2021).

[24]V. Wagner, "Pulse Shape Analysis for the GERDA Experiment to Set a New Limit on the Half-life of $0\nu\beta\beta$ Decay of Ge^{76}", PhD thesis (Ruperto-Carola-University of Heidelberg, 2017).

[25]M. Agostini et al. (GERDA), "Production, characterization and operation of ^{76}Ge enriched BEGe detectors in GERDA", Eur. Phys. J. C **75**, 39 (2015).

[26]A. W. Schardt and J. P. Welker, "Energy Levels of As^{75}", Phys. Rev. **99**, 810–824 (1955).

[27]M. Boswell et al., "MaGe-a Geant4-based Monte Carlo Application Framework for Low-background Germanium Experiments", IEEE Trans. Nucl. Sci. **58**, 1212–1220 (2011).

[28]J. Huang, "An Exploratory Search for Neutron Disappearance in GERDA", Internal presentation, (2020).

[29]H.-S. Wu, "Low Energy Calibration for GERDA and Light Yield Enhancement of Wavelength-Shifters and Reflectors", MA thesis (University of Zurich, 2021).

[30]R. Mingazheva, "Calibration,vBackground Study, and Search for New Physics with the GERDA Experiment", PhD thesis (University of Zurich, 2019).

[31]J. Huang, "Statistics", Internal report, (2020).

[32]C. Dormann, *Parametrische Statistik*, Statistik und ihre Anwendungen (Springer Spektrum, 2013), pp. 7, 55.

[33]R. Hiptmair, *Numerical methods for computational science and engineering*, tech. rep. (SAM, ETH Zurich, Autumn Term 2020), pp. 529, 533, 750.

[34]LEGEND-Collaboration, LEGEND, `https://legend-exp.org/`, (accessed: 18.08.2021).

8 Appendix

8.1 Efficiency Table

Detector	GD91A	GD35B	GD02B	GD00B	GD61A	GD89B	GD02D
GD91A		1.6e-03	3.3e-05	1.4e-06	2.0e-07	0.0e+00	0.0e+00
GD35B	1.1e-03		1.2e-03	3.9e-05	8.0e-07	0.0e+00	0.0e+00
GD02B	3.2e-05	1.7e-3		1.3e-03	4.0e-05	1.2e-06	2.0e-07
GD00B	1.2e-06	4.7e-05	1.1e-03		1.3e-03	2.4e-05	1.0e-06
GD61A	0.0e+00	2.4e-06	3.4e-05	1.2e-03		1.1e-03	3.5e-05
GD89B	0.0e+00	0.0e+00	2.2e-06	3.5e-05	1.4e-03		8.2e-04
GD02D	0.0e+00	0.0e+00	0.0e+00	2.2e-06	4.4e-05	8.2e-04	
GD91C	0.0e+00	0.0e+00	0.0e+00	2.0e-07	2.8e-06	6.2e-05	3.2e-03
GD02A	1.3e-05	1.1e-05	7.4e-06	1.4e-06	6.0e-07	2.0e-07	2.0e-07
GD32B	1.2e-05	2.4e-05	2.4e-05	1.6e-05	5.2e-06	1.4e-06	6.0e-07
GD32A	5.2e-06	1.3e-05	1.5e-05	9.4e-06	3.4e-06	6.0e-07	4.0e-07
GD32C	3.8e-06	8.0e-06	1.1e-05	1.0e-05	9.0e-06	3.2e-06	1.6e-06
GD89C	1.6e-06	5.0e-06	7.6e-06	1.0e-05	1.3e-05	7.2e-06	4.0e-06
GD61C	4.0e-07	1.0e-06	4.0e-06	1.1e-05	1.3e-05	7.2e-06	5.6e-06
GD76B	0.0e+00	4.0e-07	1.2e-06	4.4e-06	8.0e-06	1.0e-05	8.4e-06
GD00C	0.0e+00	0.0e+00	6.0e-07	1.2e-06	5.2e-06	1.1e-05	8.0e-06
GD35C	6.0e-07	2.0e-07	2.0e-07	0.0e+00	2.0e-07	0.0e+00	0.0e+00
GD76C	4.0e-07	2.0e-07	2.0e-07	4.0e-07	2.0e-07	0.0e+00	0.0e+00
GD89D	0.0e+00	4.0e-07	4.6e-06	8.0e-07	0.0e+00	0.0e+00	0.0e+00
GD00D	0.0e+00	0.0e+00	0.0e+00	0.0e+00	5.4e-06	0.0e+00	0.0e+00
GD79C	0.0e+00	0.0e+00	0.0e+00	0.0e+00	5.4e-06	0.0e+00	0.0e+00
GD35A	0.0e+00	0.0e+00	0.0e+00	1.2e-06	0.0e+00	4.0e-07	1.6e-06
GD91B	0.0e+00	0.0e+00	0.0e+00	0.0e+00	4.0e-07	2.2e-06	5.0e-06
GD61B	0.0e+00	0.0e+00	0.0e+00	0.0e+00	4.0e-07	4.0e-06	5.0e-06
GD00A	1.3e-04	1.3e-04	2.3e-05	4.4e-06	1.0e-06	2.0e-07	0.0e+00
GD02C	1.1e-04	1.9e-04	6.8e-05	1.9e-05	2.2e-06	4.0e-07	0.0e+00
GD79B	4.9e-05	1.6e-04	1.3e-04	8.4e-05	1.9e-05	2.8e-06	4.0e-07
GD91D	4.6e-06	6.2e-05	1.1e-04	1.4e-04	7.6e-05	1.5e-05	1.4e-06
GD32D	2.4e-06	1.4e-05	5.6e-05	1.4e-04	1.5e-04	6.5e-05	1.2e-05
GD89A	0.0e+00	2.8e-06	1.1e-05	6.3e-05	1.5e-04	1.1e-04	5.9e-05
GTF45	8.8e-05	1.6e-04	6.8e-05	2.6e-05	3.2e-06	8.0e-07	2.0e-07
GTF32	5.2e-06	4.2e-05	8.4e-05	1.5e-04	8.7e-05	2.0e-05	3.2e-06
GTF112	0.0e+00	1.0e-06	8.4e-06	5.1e-05	1.2e-04	1.12e-04	4.9e-05
ANG5	7.5e-05	1.5e-04	6.2e-05	2.6e-05	4.6e-06	0.0e+00	2.0e-07
RGI	4.4e-06	3.1e-05	7.9e-05	1.4e-04	1.0e-04	3.5e-05	5.4e-06
ANG3	0.0e+00	0.0e+00	1.8e-06	1.3e-05	4.8e-05	9.8e-05	9.5e-05
ANG2	8.8e-06	1.0e-05	8.0e-06	5.0e-06	2.0e-06	2.0e-07	0.0e+00
RGII	8.0e-07	6.0e-06	6.8e-06	7.4e-06	1.3e-05	4.8e-06	2.6e-06
ANG4	0.0e+00	6.0e-07	1.0e-06	3.2e-06	7.6e-06	1.0e-05	1.0e-05
ANG1	0.0e+00	2.0e-07	6.0e-07	9.8e-06	4.8e-05	9.9e-05	4.5e-03

Table 7: Signal efficiency between detectors in %. The first column shows the source detectors. (I/VI)

Detector	GD91C	GD02A	GD32B	GD32A	GD32C	GD89C	GD61C
GD91A	0.0e+00	7.8e-06	1.2e-05	4.0e-06	3.8e-06	1.6e-06	4.0e-07
GD35B	0.0e+00	8.6e-06	1.1e-05	7.6e-06	9.6e-06	4.8e-06	1.4e-06
GD02B	0.0e+00	5.0e-06	6.2e-06	8.0e-06	1.6e-05	7.6e-06	3.0e-06
GD00B	2.0e-07	1.8e-06	4.6e-06	5.6e-06	1.0e-05	7.8e-06	7.8e-06
GD61A	2.6e-06	4.0e-07	3.4e-06	3.0e-06	8.0e-06	7.8e-06	9.8e-06
GD89B	6.4e-05	0.0e+00	0.0e+00	1.2e-06	4.8e-06	7.4e-06	7.4e-06
GD02D	3.3e-03	2.0e-07	0.0e+00	2.0e-07	1.0e-06	4.4e-06	6.6e-06
GD91C		0.0e+00	0.0e+00	0.0e+00	4.0e-07	1.2e-06	3.8e-06
GD02A	0.0e+00		3.7e-03	3.6e-05	7.2e-06	0.0e+00	00.0e+00
GD32B	0.0e+00	2.8e-03		4.6e-03	4.4e-03	6.5e-05	4.4e-06
GD32A	0.0e+00	4.5e-05	9.8e-04		4.3e-03	6.3e-05	4.4e-06
GD32C	2.0e-07	6.0e-06	7.0e-05	2.5e-03		1.0e-03	4.8e-05
GD89C	1.8e-06	0.0e+00	2.8e-06	5.0e-05	1.4e-03		1.4e-03
GD61C	3.8e-06	0.0e+00	0.0e+00	3.4e-06	6.1e-05	1.3e-03	
GD76B	8.6e-06	0.0e+00	0.0e+00	6.0e-07	3.8e-06	4.2e-05	1.0e-03
GD00C	1.1e-05	0.0e+00	0.0e+00	0.0e+00	0.0e+00	4.0e-06	8.6e-05
GD35C	0.0e+00	1.1e-04	1.4e-04	2.5e-05	4.8e-06	1.2e-06	2.0e-07
GD76C	0.0e+00	1.0e-04	1.5e-04	6.0e-05	4.1e-05	6.8e-06	1.4e-06
GD89D	0.0e+00	3.6e-05	1.2e-04	9.8e-05	1.4e-04	3.9e-05	8.4e-06
GD00D	2.0e-07	6.0e-07	9.2e-06	1.3e-05	1.1e-04	1.2e-04	1.2e-04
GD79C	2.0e-07	6.0e-07	9.2e-06	1.3e-05	1.1e-04	1.2e-04	1.2e-04
GD35A	2.2e-06	0.0e+00	6.0e-07	4.2e-06	2.5e-05	7.8e-05	1.3e-04
GD91B	4.8e-06	0.0e+00	2.0e-07	6.0e-07	4.2e-06	1.8e-05	8.8e-05
GD61B	6.8e-06	0.0e+00	0.0e+00	4.0e-07	6.0e-07	3.8e-06	3.1e-05
GD00A	0.0e+00	6.0e-07	4.0e-07	2.0e-07	0.0e+00	0.0e+00	0.0e+00
GD02C	0.0e+00	0.0e+00	0.0e+00	0.0e+00	8.0e-07	2.0e-07	0.0e+00
GD79B	0.0e+00	0.0e+00	2.0e-07	2.6e-06	4.8e-06	0.0e+00	0.0e+00
GD91D	2.0e-07	2.0e-07	6.0e-07	1.2e-06	2.0e-07	2.0e-07	1.0e-06
GD32D	1.8e-06	0.0e+00	0.0e+00	2.0e-07	0.0e+00	2.8e-06	1.0e-06
GD89A	1.3e-05	0.0e+00	0.0e+00	0.0e+00	4.0e-07	6.0e-07	2.0e-07
GTF45	0.0e+00	7.4e-05	1.4e-04	5.6e-05	4.2e-05	7.4e-06	2.6e-06
GTF32	4.0e-07	3.2e-06	2.8e-05	5.4e-05	1.4e-04	9.5e-05	5.0e-05
GTF112	1.5e-05	2.0e-07	1.2e-06	2.0e-06	2.5e-05	6.8e-05	1.2e-04
ANG5	0.0e+00	7.3e-05	1.2e-04	4.7e-05	3.5e-05	8.0e-06	1.4e-06
RGI	1.6e-06	3.6e-06	2.2e-05	4.0e-05	1.3e-04	1.1e-04	6.2e-05
ANG3	5.1e-05	2.0e-07	4.0e-07	1.0e-06	6.8e-06	2.2e-05	7.6e-05
ANG2	00.0e+00	6.2e-06	7.2e-06	6.0e-06	5.2e-06	3.0e-06	0.0e+00
RGII	4.0e-07	2.0e-06	5.2e-06	5.0e-06	9.4e-06	7.2e-06	7.4e-06
ANG4	8.2e-06	2.0e-07	6.0e-07	4.0e-07	3.6e-06	4.4e-06	7.4e-06
ANG1	7.4e-05	0.0e+00	0.0e+00	0.0e+00	2.0e-07	0.0e+00	8.0e-07

Table 8: Signal efficiency between detectors in %. The first column shows the source detectors. (II/VI)

Detector	GD76B	GD00C	GD35C	GD76C	GD89D	GD00D	GD79C
GD91A	0.0e+00	0.0e+00	6.0e-07	4.0e-07	0.0e+00	0.0e+00	0.0e+00
GD35B	0.0e+00	2.0e-07	2.0e-07	0.0e+00	0.0e+00	1.2e-06	2.0e-07
GD02B	8.0e-07	2.0e-07	0.0e+00	0.0e+00	5.6e-06	1.2e-06	2.0e-07
GD00B	3.6e-06	2.4e-06	0.0e+00	1.0e-06	4.0e-07	0.0e+00	2.0e-07
GD61A	4.2e-06	6.2e-06	0.0e+00	0.0e+00	0.0e+00	6.0e-07	6.6e-06
GD89B	3.8e-06	1.0e-05	0.0e+00	0.0e+00	0.0e+00	8.0e-07	0.0e+00
GD02D	4.8e-06	1.3e-05	0.0e+00	0.0e+00	0.0e+00	0.0e+00	0.0e+00
GD91C	4.0e-06	2.0e-05	0.0e+00	0.0e+00	0.0e+00	0.0e+00	0.0e+00
GD02A	0.0e+00	0.0e+00	1.5e-04	1.6e-04	3.2e-05	8.6e-06	1.0e-06
GD32B	0.0e+00	0.0e+00	1.5e-04	3.0e-04	1.8e-04	1.8e-04	3.8e-05
GD32A	0.0e+00	0.0e+00	2.7e-05	1.2e-04	1.1e-04	1.4e-04	3.1e-05
GD32C	8.0e-07	4.0e-07	6.8e-06	4.3e-05	9.4e-05	1.8e-04	1.1e-04
GD89C	2.4e-05	8.e-06	1.2e-06	1.2e-05	4.0e-05	1.4e-04	1.9e-04
GD61C	5.6e-04	1.1e-04	0.0e+00	2.6e-06	4.4e-06	5.7e-05	1.6e-04
GD76B		4.7e-03	0.0e+00	4.0e-07	8.0e-07	8.8e-06	5.4eE-05
GD00C	1.9e-03		0.0e+00	2.0e-07	0.0e+00	1.8e-06	1.1e-05
GD35C	0.0e+00	0.0e+00		4.0e-03	4.9e-05	4.4e-06	4.0e-07
GD76C	4.0e-07	8.0e-07	3.1e-03		8.4e-04	6.3e-05	2.8e-06
GD89D	4.0e-07	4.0e-07	6.3e-05	1.5e-03		1.8e-03	5.7e-05
GD00D	2.4e-05	1.4e-05	6.0e-07	3.4e-06	2.7e-05		3.9e-03
GD79C	2.4e-05	1.4e-05	6.0e-07	3.4e-06	2.7e-05	1.6e-03	
GD35A	5.7e-05	6.5e-05	0.0e+00	2.0e-07	1.6e-06	4.8e-05	1.4e-03
GD91B	7.8e-05	1.6e-04	0.0e+00	0.0e+00	2.0e-07	3.8e-06	3.6e-05
GD61B	4.6e-05	1.8e-04	0.0e+00	0.0e+00	0.0e+00	0.0e+00	1.4e-06
GD00A	0.0e+00	0.0e+00	8.4e-06	1.2e-05	4.4e-06	3.0e-06	6.0e-07
GD02C	0.0e+00	0.0e+00	8.2e-06	1.3e-05	4.8e-06	6.4e-06	2.8e-06
GD79B	0.0e+00	2.0e-07	5.8e-06	1.2e-05	7.4e-06	1.4e-05	6.2e-06
GD91D	0.0e+00	0.0e+00	2.2e-06	7.2e-06	1.1e-05	9.6e-06	1.0e-05
GD32D	0.0e+00	0.0e+00	4.0e-07	4.2e-06	3.8e-06	1.2e-05	1.3e-05
GD89A	2.0e-07	1.6e-06	8.0e-07	4.0e-07	1.6e-06	8.0e-06	1.1e-05
GTF45	0.0e+00	2.0e-07	9.8e-05	1.6e-04	7.0e-05	4.3e-05	7.8e-06
GTF32	5.4e-06	2.0e-06	4.6e-06	2.7e-05	6.4e-05	1.8e-04	1.3e-04
GTF112	4.8e-05	5.7e-05	2.0e-07	1.2e-06	4.2e-06	2.9e-05	9.9e-05
ANG5	2.0e-07	2.0e-07	8.0e-06	1.1e-05	7.8e-06	7.0e-06	2.2e-06
RGI	9.4e-06	7.4e-06	1.8e-06	4.8e-06	5.8e-06	9.2e-06	1.2e-05
ANG3	6.3e-05	1.3e-04	2.0e-07	6.0e-07	8.0e-07	3.6e-06	5.0e-06
ANG2	2.0e-07	2.0e-07	8.8e-05	1.4e-04	6.0e-05	4.0e-05	1.0e-05
RGII	2.0e-06	1.2e-06	4.0e-06	1.7e-05	4.4e-05	1.4e-04	1.4e-04
ANG4	7.0e-06	1.5e-05	0.0e+00	2.0e-07	0.0e+00	1.2e-05	4.6e-05
ANG1	3.6e-06	9.0e-06	2.0e-07	6.0e-07	2.0e-07	3.6e-06	6.4e-06

Table 9: Signal efficiency between detectors in %. The first column shows the source detectors. (III/VI)

Detector	GD35A	GD91B	GD61B	GD00A	GD02C	GD79B	GD91D
GD91A	0.0e+00	0.0e+00	0.0e+00	9.4e-05	1.4e-04	5.1e-05	6.4e-06
GD35B	0.0e+00	0.0e+00	0.0e+00	6.6e-05	1.8e-04	1.3e-04	5.7e-05
GD02B	6.0e-07	0.0e+00	0.0e+00	1.5e-05	9.3e-05	1.6e-04	1.3e-04
GD00B	8.0e-07	0.0e+00	2.0e-07	2.6e-06	2.4e-05	9.2e-05	1.4e-04
GD61A	4.0e-07	0.0e+00	6.0e-07	2.0e-07	2.6e-06	1.8e-05	7.2e-05
GD89B	0.0e+00	2.8e-06	5.8e-06	2.0e-07	1.0e-06	3.0e-06	1.8e-05
GD02D	2.6e-06	3.4e-06	7.2e-06	0.0e+00	2.0e-07	0.0e+00	2.0e-06
GD91C	3.8e-06	7.0e-06	8.2e-06	0.0e+00	2.0e-07	2.0e-07	0.0e+00
GD02A	0.0e+00	0.0e+00	0.0e+00	2.0e-07	4.0e-07	0.0e+00	0.0e+00
GD32B	6.0e-06	1.0e-06	4.0e-07	4.0e-07	2.0e-07	4.4e-06	2.8e-06
GD32A	5.0e-06	8.0e-07	4.0e-07	0.0e+00	2.0e-07	4.4e-06	1.8e-06
GD32C	2.4e-05	3.0e-06	6.0e-07	0.0e+00	4.0e-07	3.4e-06	0.0e+00
GD89C	1.2e-04	2.4e-05	5.8e-06	0.0e+00	4.0e-07	4.0e-07	2.0e-07
GD61C	1.8e-04	9.8e-05	2.9e-05	0.0e+00	0.0e+00	0.0e+00	8.0e-07
GD76B	1.4e-04	1.5e-04	1.0e-04	0.0e+00	0.0e+00	0.0e+00	0.0e+00
GD00C	5.5e-05	1.3e-04	1.5e-04	0.0e+00	0.0e+00	0.0e+00	0.0e+00
GD35C	0.0e+00	0.0e+00	0.0e+00	9.0e-06	8.0e-06	8.6e-06	1.0e-06
GD76C	0.0e+00	0.0e+00	0.0e+00	5.0e-06	1.1e-05	1.0e-05	6.2e-06
GD89D	3.4e-06	6.0e-07	0.0e+00	3.4e-06	8.2e-06	1.0e-05	1.3e-05
GD00D	1.4e-03	2.9e-05	1.0e-06	2.0e-07	2.4e-06	5.4e-06	1.0e-05
GD79C	1.4e-03	2.9e-05	1.0e-06	2.0e-07	2.4e-06	5.4e-06	1.0e-05
GD35A		1.3e-03	4.6e-05	4.0e-07	8.0e-07	2.4e-06	6.0e-06
GD91B	1.6e-03		1.6e-03	0.0e+00	4.0e-07	1.0e-06	3.6e-06
GD61B	4.5e-05	1.4e-03		0.0e+00	0.0e+00	2.0e-07	1.2e-06
GD00A	2.0e-07	0.0e+00	0.0e+00		4.0e-03	7.2e-05	2.8e-06
GD02C	8.0e-07	2.0e-07	0.0e+00	2.2e-03		1.4e-03	5.2e-05
GD79B	2.6e-06	4.0e-07	4.0e-07	4.8e-05	1.5e-03		1.6e-03
GD91D	6.2e-06	2.0e-06	1.2e-06	2.6e-06	5.8e-05	1.6e-03	
GD32D	1.1e-05	5.6e-06	2.4e-06	4.0e-07	1.6e-06	4.7e-05	1.5e-03
GD89A	1.4e-05	8.0e-06	9.2e-06	0.0e+00	0.0e+00	4.0e-07	4.0e-05
GTF45	8.0e-07	4.0e-07	0.0e+00	6.3e-05	1.6e-04	1.1e-04	3.9e-05
GTF32	4.0e-05	4.6e-06	1.4e-06	2.8e-06	2.1e-05	8.4e-05	1.5e-04
GTF112	1.8e-04	9.1e-05	3.3e-05	0.0e+00	2.0e-07	3.8e-06	3.0e-05
ANG5	8.0e-07	4.0e-07	2.0e-07	5.4e-06	1.0e-05	8.2e-06	6.0e-06
RGI	1.0e-05	2.6e-06	8.0e-07	1.2e-06	3.2e-06	8.0e-06	9.6e-06
ANG3	1.0e-05	1.2e-05	1.3e-05	0.0e+00	0.0e+00	1.0e-06	1.6e-06
ANG2	1.2e-06	4.0e-07	0.0e+00	6.4e-05	1.5e-04	9.5e-05	3.3e-05
RGII	5.8e-05	1.7e-05	3.2e-06	8.0e-07	1.9e-05	5.9e-05	1.2e-04
ANG4	1.1e-04	1.3e-04	8.6e-05	0.0e+00	0.0e+00	2.2e-06	8.8e-06
ANG1	1.1e-05	1.2e-05	1.4e-05	0.0e+00	0.0e+00	0.0e+00	8.0e-07

Table 10: Signal efficiency between detectors in %. The first column shows the source detectors. (IV/VI)

Detector	GD32D	GD89A	GTF45	GTF32	GTF112	ANG5	RGI
GD91A	2.2e-06	0.0e+00	1.0e-06	2.3e-05	5.5e-04	3.8e-04	1.3e-05
GD35B	1.2e-05	1.8e-06	4.2e-06	1.4e-04	7.9e-04	5.4e-04	8.3e-05
GD02B	7.1e-05	5.2e-06	3.6e-05	4.2e-04	4.3e-04	3.0e-04	2.6e-04
GD00B	1.6e-04	5.1e-05	2.0e-04	6.5e-04	1.3e-04	1.0e-04	4.8e-04
GD61A	1.6e-04	9.4e-05	5.2e-04	3.4e-04	2.0e-05	1.8e-05	3.2e-04
GD89B	8.6e-05	9.8e-05	6.2e-04	9.4e-05	3.0e-06	2.0e-06	1.2e-04
GD02D	1.7e-05	4.7e-05	2.4e-04	1.5e-05	8.0e-07	6.0e-07	2.6e-05
GD91C	3.2e-06	1.1e-05	7.8e-05	1.8e-06	0.0e+00	2.0e-07	5.6e-06
GD02A	0.0e+00	0.0e+00	1.2e-06	1.9e-05	5.6e-04	4.2e-04	1.4e-05
GD32B	0.0e+00	0.0e+00	2.3e-05	4.7e-04	1.3e-03	8.6e-04	2.6e-04
GD32A	0.0e+00	0.0e+00	1.7e-05	3.6e-04	5.0e-04	3.3e-04	1.9e-04
GD32C	0.0e+00	2.0e-07	1.0e-04	6.0e-04	2.1e-04	1.3e-04	4.1e-04
GD89C	2.2e-06	8.0e-07	3.8e-04	5.3e-04	5.8e-05	4.3e-05	4.6e-04
GD61C	1.8e-06	0.0e+00	6.8e-04	2.2e-04	6.6e-06	8.0e-06	2.3e-04
GD76B	0.0e+00	2.0e-07	4.2e-04	4.2e-05	1.0e-06	1.6e-06	7.2e-05
GD00C	2.0e-07	1.0e-06	2.0e-04	9.8e-06	1.0e-06	6.0e-07	2.1e-05
GD35C	1.4e-06	2.0e-07	6.0e-07	1.6e-05	6.0e-04	3.4e-05	3.8e-06
GD76C	3.2e-06	4.0e-07	2.8e-06	9.9e-05	8.0e-04	3.9e-05	1.2e-05
GD89D	7.4e-06	2.6e-06	2.3e-05	3.9e-04	5.7e-04	3.8e-05	2.7e-05
GD00D	1.1e-05	7.8e-06	4.1e-04	4.8e-04	3.8e-05	8.4e-06	3.0e-05
GD79C	1.1e-05	7.8e-06	4.1e-04	4.8e-04	3.8e-05	8.4e-06	3.0e-05
GD35A	9.6e-06	7.2e-06	6.4e-04	1.6e-04	3.2e-06	4.0e-06	2.4e-05
GD91B	6.6e-06	7.0e-06	3.9e-04	3.0e-05	1.2e-06	1.2e-06	1.2e-05
GD61B	2.2e-06	4.8e-06	1.3e-04	5.4e-06	0.0e+00	6.0e-07	4.6e-06
GD00A	0.0e+00	0.0e+00	4.0e-07	1.9e-05	5.9e-04	3.9e-05	6.0e-06
GD02C	2.2e-06	0.0e+00	2.2e-06	8.6e-05	7.8e-04	3.9e-05	1.1e-05
GD79B	5.0e-05	1.0e-06	2.2e-05	3.3e-04	5.7e-04	3.3e-05	2.4e-05
GD91D	1.6e-03	2.9e-05	1.2e-04	6.3e-04	2.2e-04	2.5e-05	3.4e-05
GD32D		9.7e-04	3.8e-04	5.1e-04	5.4e-05	1.1e-05	3.6e-05
GD89A	1.5e-03		6.9e-04	2.1e-04	8.2e-06	5.0e-06	2.6e-05
GTF45	7.4e-06	1.0e-06		6.2e-04	3.9e-03	4.5e-04	6.5e-05
GTF32	1.3e-04	3.2e-05	9.6e-04		8.1e-04	9.0e-05	4.3e-04
GTF112	9.7e-05	1.0e-04	3.9e-03	8.9e-04		3.8e-06	1.6e-04
ANG5	4.0e-06	6.0e-07	3.6e-06	9.4e-05	6.2e-04		2.9e-04
RGI	9.4e-06	6.8e-06	1.9e-04	5.5e-04	1.1e-04	3.4e-04	
ANG3	4.0e-06	6.0e-06	3.6e-04	4.7e-05	2.0e-06	2.0e-07	2.3e-04
ANG2	1.0e-05	8.0e-07	5.2e-06	1.0e-04	6.0e-04	0.0e+00	2.2e-06
RGII	1.4e-04	3.7e-05	1.8e-04	5.3e-04	1.0e-04	1.6e-06	2.8e-06
ANG4	4.0e-05	6.2e-05	3.8e-04	5.2e-05	2.6e-06	0.0e+00	1.0e-06
ANG1	3.3e-05	6.8e-04	3.2e-04	2.3e-05	4.0e-07	6.0e-07	1.2e-05

Table 11: Signal efficiency between detectors in %. The first column shows the source detectors. (V/VI)

Detector	ANG3	ANG2	RGII	ANG4	ANG1
GD91A	2.0E-07	4.0E-05	4.6E-06	8.0E-07	0.0E+00
GD35B	1.6E-06	4.5E-05	1.0E-05	1.6E-06	4.0E-07
GD02B	9.0E-06	3.4E-05	2.6E-05	6.6E-06	8.0E-07
GD00B	6.2E-05	2.2E-05	3.6E-05	1.6E-05	1.1E-05
GD61A	1.9E-04	8.6E-06	3.1E-05	2.7E-05	6.0E-05
GD89B	4.6E-04	1.8E-06	1.9E-05	4.1E-05	1.6E-04
GD02D	4.1E-04	1.0E-06	6.2E-06	4.4E-05	1.8E-04
GD91C	2.3E-04	2.0E-07	3.0E-06	3.0E-05	1.2E-04
GD02A	6.0E-07	3.9E-05	4.8E-06	1.0E-06	0.0E+00
GD32B	6.8E-06	8.1E-05	3.7E-05	5.8E-06	0.0E+00
GD32A	5.4E-06	4.0E-05	2.6E-05	3.6E-06	0.0E+00
GD32C	2.4E-05	2.4E-05	3.0E-05	8.8E-06	0.0E+00
GD89C	1.2E-04	1.4E-05	3.0E-05	2.2E-05	2.0E-07
GD61C	3.2E-04	4.2E-06	2.5E-05	3.5E-05	1.0E-06
GD76B	5.2E-04	1.2E-06	1.2E-05	5.4E-05	9.0E-06
GD00C	4.0E-04	4.0E-07	4.0E-06	3.8E-05	8.8E-06
GD35C	6.0E-07	4.7E-04	8.6E-06	2.0E-07	0.0E+00
GD76C	1.4E-06	5.5E-04	5.2E-05	1.8E-06	4.0E-07
GD89D	2.8E-06	4.1E-04	2.0E-04	8.4E-06	1.4E-06
GD00D	2.0E-05	3.4E-05	3.8E-04	1.5E-04	6.8E-06
GD79C	2.0E-05	3.4E-05	3.8E-04	1.5E-04	6.8E-06
GD35A	3.3E-05	4.2E-06	1.4E-04	3.8E-04	1.3E-05
GD91B	4.2E-05	1.0E-06	4.6E-05	5.2E-04	2.0E-05
GD61B	3.9E-05	0.0E+00	8.2E-06	3.1E-04	1.5E-05
GD00A	2.0E-07	4.7E-04	1.1E-05	2.0E-07	0.0E+00
GD02C	2.0E-07	5.5E-04	5.0E-05	1.4E-06	0.0E+00
GD79B	2.4E-06	4.0E-04	1.8E-04	7.4E-06	0.0E+00
GD91D	9.4E-06	1.5E-04	3.7E-04	3.7E-05	1.4E-06
GD32D	2.0E-05	4.7E-05	3.8E-04	1.4E-04	3.6E-05
GD89A	3.1E-05	6.6E-06	1.9E-04	3.7E-04	1.2E-03
GTF45	1.2E-06	4.7E-04	4.9E-05	1.0E-06	0.0E+00
GTF32	3.7E-05	9.9E-05	3.8E-04	4.3E-05	8.0E-06
GTF112	3.0E-04	2.8E-06	1.4E-04	3.4E-04	9.7E-05
ANG5	4.0E-07	1.2E-06	1.0E-06	0.0E+00	6.0E-07
RGI	2.5E-04	2.0E-06	1.2E-06	2.0E-07	5.0E-06
ANG3		0.0E+00	2.0E-07	1.5E-05	1.5E-05
ANG2	0.0E+00		2.6E-04	0.0E+00	2.0E-07
RGII	4.0E-07	3.6E-04		3.1E-04	1.3E-05
ANG4	1.5E-05	2.0E-07	2.7E-04		1.7E-04
ANG1	4.5E-05	8.0E-07	3.5E-05	5.0E-04	

Table 12: Signal efficiency between detectors in %. The first column shows the source detectors. (VI/VI)